

Development of a Low-Frequency Vibration-Assisted Drilling Device for Difficult-to-Cut Materials

Feng Jiao (✉ jiaofeng@hpu.edu.cn)

Henan Polytechnic University <https://orcid.org/0000-0002-8553-5789>

Yuanxiao Li

Dong Wang

Jinglin Tong

Ying Niu

Research Article

Keywords: Low-frequency vibration-assisted drilling, Ring flexure hinge, Titanium alloy, Carbon fiber reinforced plastic

Posted Date: March 4th, 2021

DOI: <https://doi.org/10.21203/rs.3.rs-269153/v1>

License:  This work is licensed under a Creative Commons Attribution 4.0 International License.

[Read Full License](#)

Version of Record: A version of this preprint was published at The International Journal of Advanced Manufacturing Technology on July 21st, 2021. See the published version at <https://doi.org/10.1007/s00170-021-07668-1>.

Development of a low-frequency vibration-assisted drilling device for difficult-to-cut materials

Feng Jiao^{1,a*}, Yuanxiao Li^{1,b}, Dong Wang^{1,c}, Jinglin Tong^{1,d}, Ying Niu^{1,e}

(1.School of Mechanical and Power Engineering, Henan Polytechnic University, Jiaozuo 454000, Henan, China)

^ajiaofeng@hpu.edu.cn; ^bliyuanxiao9@163.com; ^caton.wd@gmail.com; ^dtongjinglin@hpu.edu.cn;

^eniuying@hpu.edu.cn; *Corresponding author.

Abstract: In the drilling process of difficult-to-cut materials, conventional drilling has resulted in various problems such as high drilling temperature and poor machining quality. Low-frequency vibration-assisted drilling has great potential in overcoming these problems since broken chips are generated. In order to promote the application of low-frequency vibration-assisted drilling device in machining difficult-to-cut materials. In this paper, a low-frequency vibration-assisted drilling device is developed by using a novel ring flexure hinge as the elastic recovery mechanism. First, based on the theory of elastic mechanics and mechanical vibration, the stiffness of the ring flexure hinge is designed theoretically, and the influence of its structural parameters on its deflection is analyzed. And then the correctness of the theoretical design is further verified by static and dynamic simulation and stiffness test. Finally, the vibration performance of the device is tested under no-load condition, and the actual drilling test is conducted to verify the drilling performance. The results show that the device could realize the axial low-frequency vibration with constant frequency-to-rotation ratio and amplitude stepless adjustment and present good working stability under no-load and load conditions. In the actual drilling test of titanium alloy and carbon fiber reinforced plastic (CFRP)/ titanium alloy laminated structure, the device under appropriate processing parameters breaks the titanium alloy chip into small pieces and reduces the drilling temperature by 44% and inhibits the secondary damage of CFRP. It is demonstrated that the device could meet the actual processing requirements. And it also provides guidance for the design of low-frequency vibration-assisted drilling device.

Keywords: Low-frequency vibration-assisted drilling; Ring flexure hinge; Titanium alloy; Carbon fiber reinforced plastic

1 Introduction

Difficult-to-cut materials such as titanium alloy, high temperature alloy and composite materials have a great prospect in aerospace and aircraft manufacturing. Due to tens of thousands of holes to be drilled to meet the mechanical bolting or riveting demand for aircraft assembly, it is still a challenge to make holes on the difficult-to-cut materials with high quality [1, 2].

The machining difficulties of the difficult-to-cut materials have been reported, such as delamination damage during drilling of CFRP and CFRP/titanium alloy stacked materials [3], chip evacuation during drilling, and low thermal conductivity combined with a high chemical affinity of titanium alloys [4, 5]. These machinability problems lead to high machining temperature, short tool life and poor machining quality.

Compared with conventional drilling (CD), vibration-assisted drilling has great potential in reducing cutting temperature, prolonging tool life and improving machining quality [6, 7]. According to the frequency of vibration, there are low-frequency vibration-assisted drilling (LFVAD) and ultrasonic vibration-assisted drilling (UVAD). UVAD has significant technological effects in the processing of difficult-to-cut materials [8-10]. However, in ultrasonic vibration drilling, the vibration amplitude can reach several microns, which restricts the machining efficiency [11, 12]. LFVAD process with appropriate processing and vibration parameters becomes an intermittent cutting, which has more advantages in chip breaking and chip removal, reducing drilling temperature and improving processing efficiency [13-17].

Some scholars have applied LFVAD to the processing of aluminum alloy, titanium alloy and carbon fiber reinforced plastic (CFRP)/titanium (aluminum) stacked materials. Pecat O. [18, 19] developed a kinematic model of the vibration assisted drilling process for a two-fluted cutter and studied the chip shape under different processing parameters and vibration parameters through LFVAD experiment. It was found that the tool wear as well as the cutting temperatures were significantly decreased by the application of LFVAD, whereas the thrust force was raised compared to CD. Okamura K. [20] carried out the experiment of LFVAD of titanium alloy. The results showed that the drilling temperature of titanium alloy decreased greatly and the drill wear

rate was suppressed largely by applying low-frequency vibration. Besides, the chip was divided into short length and the hole exit burr height and thickness became small under LFVAD. As the amplitude becomes large and the vibration frequency becomes high, these effects appear more remarkably. Hussein R. [21] carried out the experiment of LFVAD of CFRP/Ti6Al4V stacked material and found that the temperature of LFVAD was significantly lower than that of CD. The delamination defects at the entry and exit of the CFRP were significantly improved due to an enhancement in the chip evacuation mechanism and a reduction in the cutting temperature. In addition, LFVAD could significantly reduce tool wear, but the mechanical load was larger than that of CD.

Numerous significant studies have shown that LFVAD has great potential in machining difficult-to-cut materials. Low frequency vibration-assisted drilling device is the basis of experimental research on LFVAD. At present, low-frequency vibration-assisted drilling device mainly adopts mechanical, electromagnetic and hydraulic modes [22]. The electromagnetic vibration drilling device has simple structure and high vibration frequency. However, it is only suitable for small hole machining because of its small power. The hydraulic vibration drilling device has the advantages of long life, low noise, high output power and good buffering effect, while its structure is complex and its manufacturing cost is high. The mechanical vibration drilling device has the advantages of simple structure, good rigidity and long service life. However, the cam mechanism, eccentric wheel mechanism and crank slider mechanism are often used in the vibration device [23, 24], which makes the amplitude adjustment inconvenient and requires additional power supply. Meanwhile, spring is generally used as the elastic recovery mechanism in these devices, resulting in weak rigidity of the process system and poor amplitude stability in vibration drilling, which limits the application of vibration drilling technology.

In order to promote the application of LFVAD, Laporte S [25] has developed a mechanical low-frequency vibration drilling device, which uses the spring pile as the elastic recovery mechanism of the device and needs pins to transfer torque to rotate the tool. The stiffness of elastic recovery mechanism of the device is adjusted by changing the material and number of elastic washers. And linear bearing is adopted to ensure the axial transmission of low-frequency vibration of the device. While in this paper, a

novel ring flexure hinge is used as elastic recovery mechanism to develop the low-frequency vibration-assisted drilling device through theoretical design, static and dynamic simulation and stiffness test. The ring flexure hinge can be machined with different stiffness according to the working requirements by change the structural parameters of the ring flexure hinge. In addition, the ring flexure hinge transfers torque to rotate the vibration output part and also provides guidance for the axial vibration, which makes the whole structure more compact. The LFVAD device could be directly installed on the spindle of machine tool, and with the rotation of the spindle, it could realize the axial low-frequency vibration with constant frequency-to-rotation ratio and amplitude stepless adjustment. The vibration performance of the device is tested under no-load condition, and the actual drilling test of titanium alloy and CFRP/ titanium alloy laminated structure is conducted to verify the drilling performance.

2 Working principle of the LFVAD device

The low-frequency vibration system composition and schematic diagram of the LFVAD device are shown in Fig. 1 and Fig.

2.

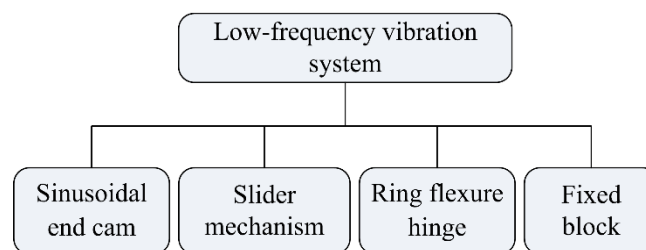


Fig. 1 The low-frequency vibration system composition

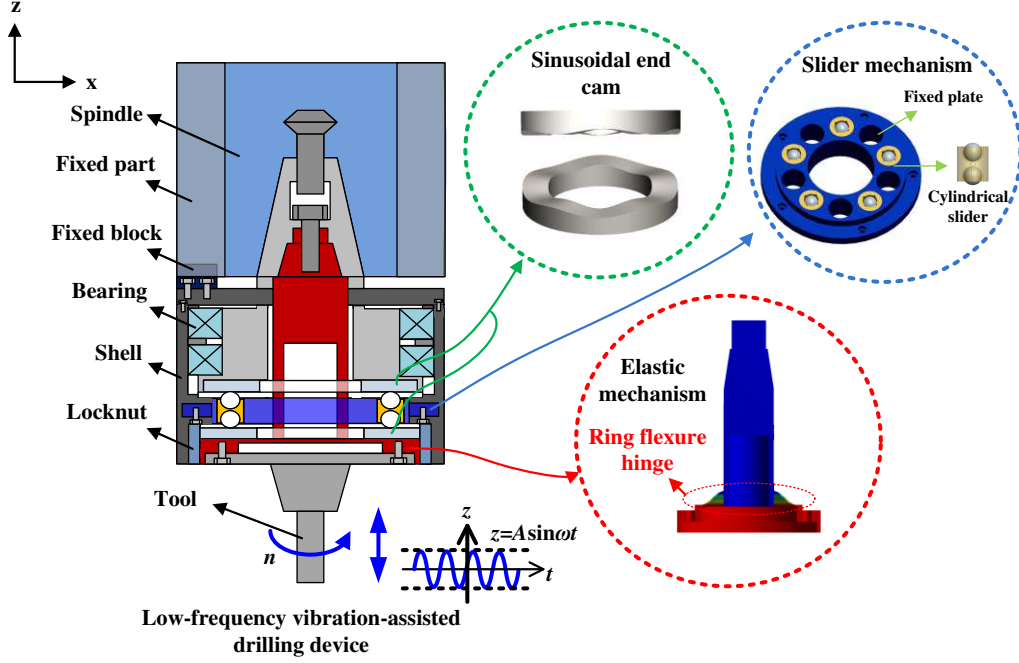


Fig. 2 The schematic diagram of the LRVAD device

The low-frequency vibration system mainly includes four parts: sinusoidal end cam, slider mechanism, ring flexure hinge and fixed block, which are integrated into BT40 tool holder.

Sinusoidal end cam, as the excitation of low-frequency vibration system, determines the amplitude range and frequency-to-rotation ratio of the device. As shown in Fig. 2, a sinusoidal curved surface is processed on one side of the ring plate. The axial low-frequency vibration of the tool is the result of the superposition of two cams with the same sinusoidal surface and the axial vibration displacement equation of the tool can be expressed as follows:

$$A = \sqrt{2(1 - \cos \varphi)} A_0 \cos(\omega t + \psi) \quad (1)$$

where A is the axial amplitude of the device, A_0 is the amplitude of a single sinusoidal surface, ω is the circular frequency of vibration, φ is the phase difference between the sinusoidal surface of the upper and lower end cams and ψ is the phase angle of tool vibration.

The stepless adjustment of the low-frequency amplitude in the range of $0-2A_0$ is realized by changing the phase difference between the two cams. The low-frequency vibration system mainly plays the role of chip breaking in the drilling process. For

common double-edged twist drill, the chip breaking condition [26] is:

$$\frac{4A}{f_r} \geq \frac{1}{\left| \sin\left(\frac{\omega_f \pi}{2}\right) \right|} \quad (2)$$

where f_r is the feed rate and ω_f is the frequency-to-rotation ratio.

When the feed rate f_r satisfies $4A/f_r > 1$, the frequency-to-rotation ratio needs to meet certain conditions to realize the theoretical chip breaking. When $4A/f_r < 1$, no matter how the frequency-to-rotation ratio is changed, the chip will not break theoretically. Therefore, the low-frequency amplitude A of the designed device must satisfy $A > f_r/4$. In addition, the number of cycles of the upper and lower sinusoidal end cams and the number of cylindrical sliders are both designed as odd numbers, that is, the frequency-to-rotation ratio ω_f is odd number. Considering the overall structure and size of the device, the number of cycles of the sinusoidal surface is set to 5 and the amplitude of sinusoidal surface is set to 0.05 mm.

As the transmission mechanism, slider mechanism includes a fixed plate with several through holes and cylindrical sliders. In order to ensure that the tool vibrates along the axis without radial vibration, the number of cylindrical sliders in the fixed plate should be equal to the number of periods of sinusoidal surface. The structure of the fixed plate and the cylindrical slider is as shown in Fig. 2. Five identical cylindrical sliders are placed in five through holes of fixed plate. Two hemispherical grooves are machined on the top and bottom of the cylindrical slider respectively. A steel ball is placed in each groove. The upper steel ball of the cylindrical slider is in contact with the upper sinusoidal end cam, and the lower steel ball is in contact with the lower sinusoidal end cam. The cylindrical slider can move axially along the through hole wall of the fixed plate, which is fixed with the outer shell by screw.

As the elastic recovery mechanism, the ring flexure hinge provides elastic restoring force for the axial vibration of the system. The detailed design and analysis of the ring flexure hinge will be carried out in the next section.

The LfvAD device can be directly installed on the spindle of machine tool. With the rotation of the spindle, the upper sinusoidal end cam rotates with the BT40 tool holder, providing harmonic excitation. The shell of the device is connected with

the fixed part of the machine tool by fixed block and does not rotate during operation. The fixed plate of the slider mechanism is connected with the shell of the device by screws, and the cylindrical slider of the slider mechanism slides up and down along the through-hole of the fixed plate under harmonic excitation. The amplitude of harmonic excitation can be changed by adjusting the phase difference between the lower sinusoidal end cam and the upper sinusoidal end cams by turning the lock nut. The frequency of harmonic excitation is related to the number of sinusoidal period (frequency-to-rotation ratio) and the spindle speed of machine tool. The ring flexure hinge provides the restoring force of harmonic excitation and makes the same harmonic vibration at the same time. Through the cooperation of the slider mechanism, the double sinusoidal end cam and the ring flexure hinge, the tool can generate axial low-frequency harmonic vibration while rotating at high speed.

According to the above, the LFVAD device could realize the low-frequency vibration with constant frequency-to-rotation ratio and amplitude stepless adjustment of the cutting tool.

3 Design of ring flexure hinge

3.1 Design principle of the ring flexure hinge

The flexure hinges are formed by the middle elastic deformation unit connecting two rigid bodies, and the relative movement between the two rigid bodies is achieved through the deformation of the intermediate unit [27]. Flexure hinges have the advantages of no mechanical friction, no clearance, compactness and high motion sensitivity. Therefore, in some mechanisms, it often replaces the spring to realize the relative motion of the internal structure of the device [28, 29]. The LFVAD device adopts a novel ring flexure hinge as elastic recovery mechanism, and the material of the ring flexure hinge is 65Mn spring steel. From Fig. 3, it can be seen that the ring flexure hinge is located at the bottom of the connecting rod. The ring flexure hinge can be regarded as a thin ring plate. The inner ring of the thin ring plate is connected with the connecting rod, and the outer ring of the thin ring plate is connected with a large thick ring, which has a large rigidity. Therefore, the vertical downward concentrated

force or uniform load acting on the thick ring surface can be approximately transformed into the transverse shear force acting on the joint of thin plate and thick ring. The axial stiffness of the ring flexure hinge is small, and the corresponding axial elastic deformation will be generated under the action of axial force, providing the elastic restoring force for the device.

Because the ring flexure hinge works in the non-resonant condition, the excitation frequency must be less than the natural frequency of the ring flexure hinge. Otherwise, the springback of ring flexure hinges will not be timely, resulting in collision and resonance. The steel balls in the cylindrical slider need to bear axial forces during operation. In order to minimize the friction and wear between the steel balls and the double end cams as well as the impact of low-frequency vibration on the machine tool spindle, the axial stiffness of the ring flexure hinge should not be too large. Therefore, the design of ring flexure hinge is mainly to make its axial stiffness meet the above two conditions at the same time.

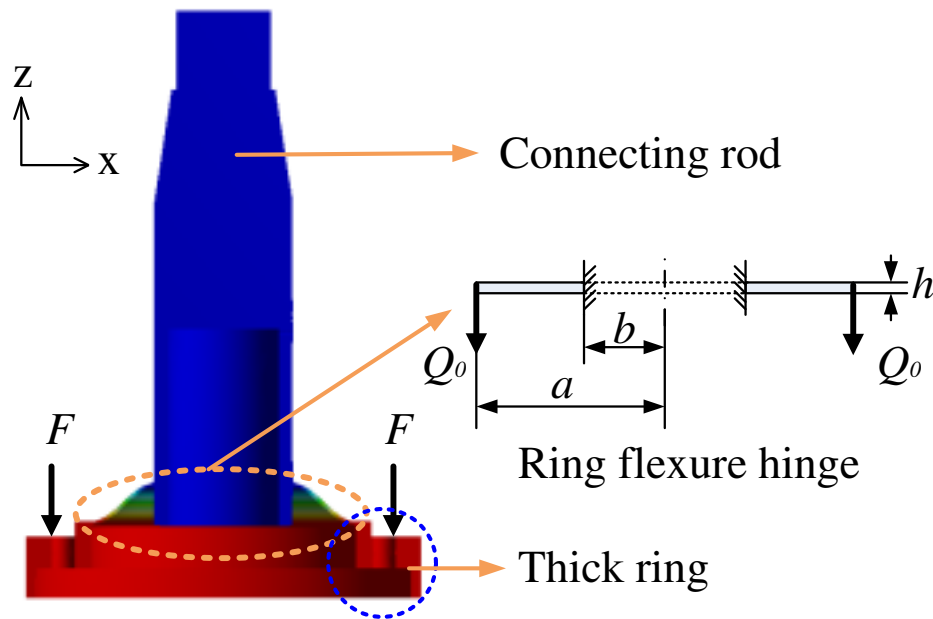


Fig. 3 The section of elastic recovery mechanism

As shown in Fig. 3, the ring flexure hinge is simplified to a ring thin plate model for axial stiffness analysis. The inner ring radius is b , the outer ring radius is a and the thickness is h .

The differential equation of circular plate bending in polar coordinate system based on the research [30] is expressed as:

$$\left(\frac{\partial^2}{\partial r^2} + \frac{1}{r} \frac{\partial}{\partial r} + \frac{1}{r^2} \frac{\partial^2}{\partial \theta^2}\right) \left(\frac{\partial^2 w}{\partial r^2} + \frac{1}{r} \frac{\partial w}{\partial r} + \frac{1}{r^2} \frac{\partial^2 w}{\partial \theta^2}\right) = \frac{q(r, \theta)}{D} \quad (3)$$

where $D = \frac{Eh^3}{12(1-\nu^2)}$ is the bending stiffness of the plate, E is the elasticity modulus of the plate, h is the thickness of the plate, ν is Poisson's ratio and q is the load.

For axisymmetric loads $q=q(r)$, because circular (ring) plates are axisymmetric in geometry, their deformation will be axisymmetric. The derivatives of deflection w to θ are all zero. The basic equation (3) of the circular plate bending is simplified to the Euler type ordinary differential equation as:

$$\left(\frac{d^2}{dr^2} + \frac{1}{r} \frac{d}{dr}\right) \left(\frac{d^2 w}{dr^2} + \frac{1}{r} \frac{dw}{dr}\right) = \frac{q(r)}{D} \quad (4)$$

The general solution of Eq. (4) can be obtained as:

$$w = Ar^2 + Br^2 \ln \frac{r}{a} + C \ln \frac{r}{a} + K + \hat{w}(r) \quad (5)$$

where a is the external radius of circular (ring) plate, $\hat{w}(r)$ is the special solution of the equation and the constants A, B, C, K are determined by the boundary conditions of the plate.

The general solution of the ring plate and the circular plate is the same. Since there is no uniformly distributed load on the ring plate, that is, $q(r)=0$, the deflection w can be expressed as:

$$w = Ar^2 + Br^2 \ln \frac{r}{a} + C \ln \frac{r}{a} + K \quad (6)$$

The inner ring of the thin ring plate is fixed with the connecting rod, and the outer ring of the thin ring plate is subjected to uniform transverse shear force Q_0 without rotation. According to the working conditions of the ring plate, two boundary conditions can be obtained as:

When $r = b$, there are:

$$w_{r=b} = 0, \frac{\partial w}{\partial r} \Big|_{r=b} = 0 \quad (7)$$

When $r = a$, there are:

$$\left(\frac{\partial w}{\partial r}\right)_{r=a} = 0, (Q)_{r=a} = -Q_0 \quad (8)$$

The internal force element formulas (bending moment, torsion and transverse shear force) of ring and circular plates are

expressed as:

$$\begin{cases} M_r = -D \left[\frac{\partial^2 w}{\partial r^2} + \nu \left(\frac{1}{r} \frac{\partial w}{\partial r} + \frac{1}{r^2} \frac{\partial^2 w}{\partial \theta^2} \right) \right] \\ M_\theta = -D \left[\left(\frac{1}{r} \frac{\partial w}{\partial r} + \frac{1}{r^2} \frac{\partial^2 w}{\partial \theta^2} \right) + \nu \frac{\partial^2 w}{\partial r^2} \right] \\ Q_r = -D \frac{\partial}{\partial r} (\nabla^2 w) \end{cases} \quad (9)$$

Substituting Eq. (7) into Eq. (6), we get following equations:

$$\begin{cases} 0 = Ab^2 + Bb^2 \ln \frac{b}{a} + C \ln \frac{b}{a} + K \\ 0 = 2Ab + 2Bb \ln \frac{b}{a} + Bb + C \frac{1}{b} \end{cases} \quad (10)$$

Substituting Eq. (8) into Eq. (8) and Eq. (9), we get following equations:

$$\begin{cases} 0 = 2Aa + Ba + C \frac{1}{a} \\ Q_0 = \frac{4DB}{a} \end{cases} \quad (11)$$

The constants A, B, C and K can be obtained by simultaneous Eq. (10) and Eq. (11), and the deflection of the ring plate can

be calculated by introducing them into Eq. (6):

$$w = Q_0 a \left[\left(\frac{r^2 \ln \left(\frac{r}{a} \right)}{4D} \right) - \frac{b^2 \left(b^2 - a^2 - 6a^2 \ln \left(\frac{b}{a} \right) \right)}{8D(a^2 - b^2)} - \frac{r^2 \left(2b^2 \ln \left(\frac{b}{a} \right) - a^2 + b^2 \right)}{8D(a^2 - b^2)} - \frac{a^2 b^2 \ln \left(\frac{b}{a} \right) \ln \left(\frac{r}{a} \right)}{2D(a^2 - b^2)} \right] \quad (12)$$

In the design process of ring flexure hinge, it is necessary to know the influence of structure parameter thickness h and inner and outer diameter on its deflection. Figure 4 shows the influence of the thickness of the ring flexure hinge on its deflection, and Figure 5 shows the relationship between the outer diameter a and deflection w when the inner diameter is determined.

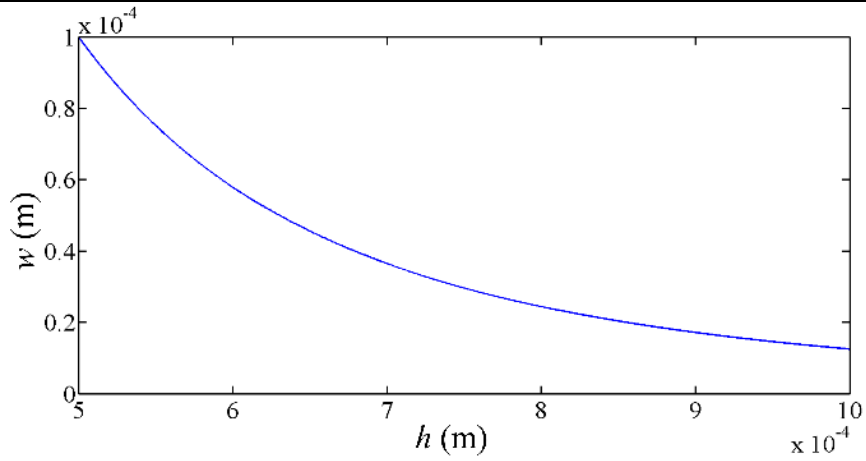


Fig. 4 Influence of thickness h

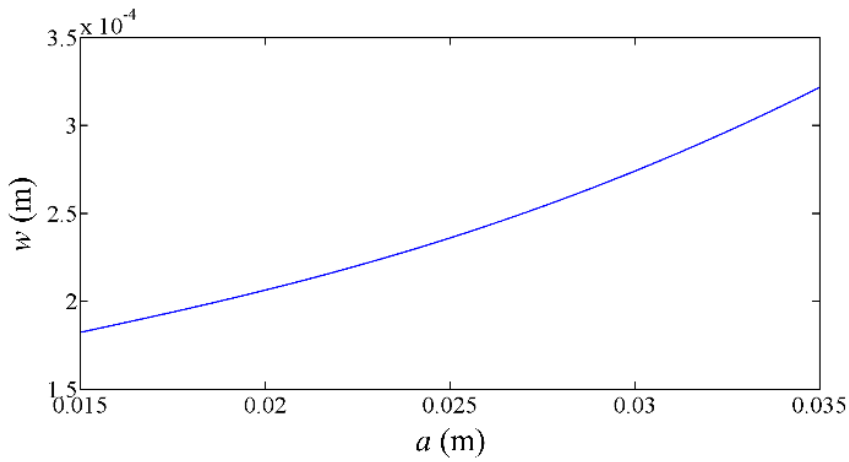


Fig. 5 Influence of outer diameter a

It can be seen from Fig. 4 and Fig. 5 that the thickness has a great influence on the deflection of the ring flexure hinge, and the deflection decreases with the increase of the thickness. In addition, with the increase of the thickness, the influence degree becomes smaller and smaller. When the inner diameter is determined, the deflection increases with the increase of the outer diameter.

Because the stiffness of the thick ring connected by the outer ring is very large, the transverse shear force acting on the outer ring of the thin ring plate can be approximately transformed into the concentrated force on the thick ring. Thus, the axial stiffness K of the ring flexure hinge can be written as:

$$K = 2\pi r Q_0 / \omega \quad (13)$$

According to the theory of mechanical vibration [31], the differential equation of undamped motion of the plate for free

vibration can be expressed as:

$$D\nabla^4 w + \rho_A \frac{\partial^2 w}{\partial t^2} = 0 \quad (14)$$

where ρ_A is the surface density of the plate.

Assuming that the plate performs a simple harmonic motion, the displacement of the plate can be expressed as:

$$w = W \cos(\omega t) \quad (15)$$

where W is the vibration mode function of the plate which is related to the coordinates and must meet the corresponding boundary conditions, and ω is the circular frequency of the vibration.

Substituting Eq. (15) into Eq. (14), we get following equations:

$$(\nabla^4 - k^4)W = 0 \quad (16)$$

$$\text{where } k^4 = \frac{\rho_A \omega^2}{D} .$$

In polar coordinate system, the Laplace operator in the Eq. (16) is expressed as:

$$\nabla^2 = \frac{\partial^2}{\partial r^2} + \frac{1}{r} \frac{\partial}{\partial r} + \frac{1}{r^2} \frac{\partial^2}{\partial \theta^2} \quad (17)$$

The total solution of Eq. (16) in polar coordinate system can be obtained as follows:

$$W(r, \theta) = \sum_{n=0}^{\infty} [A_n J_n(kr) + B_n Y_n(kr) + C_n I_n(kr) + D_n K_n(kr)] \cos n\theta + \sum_{n=1}^{\infty} [A_n^* J_n(kr) + B_n^* Y_n(kr) + C_n^* I_n(kr) + D_n^* K_n(kr)] \cos n\theta \quad (18)$$

where J_n and Y_n are Bessel functions of the first type and second type respectively; I_n and K_n are deformed Bessel functions of the first type and the second type respectively; A_n, A_n^*, \dots, D_n and D_n^* represent unknown constants related to the mode shape of circular thin plates, and their specific values are determined by boundary conditions; n is the number of pitch diameter when the circular plate vibrates.

When the origin of polar coordinates coincides with the center of the circular plate, the solution of the circular plate vibration differential equation can be simplified as follows:

$$W_n = [A_n J_n(kr) + C_n I_n(kr)] \cos n\theta \quad (19)$$

When the ring flexure hinge works, it can be regarded as the vibration of the ring plate with the inner hole boundary fixed

and the outer ring connected with the rigid mass block. Thus, the boundary conditions of the ring plate with outer diameter a and inner diameter b can be expressed as follows:

$$\begin{cases} W(b) = 0 \\ \frac{\partial W(b)}{\partial r} = 0 \end{cases} \quad (20)$$

Therefore, the circular frequency of the transverse vibration of the ring plate can be calculated as follows:

$$\omega = \frac{a_{ns}}{b^2} \sqrt{\frac{D}{\rho_A}} \quad (21)$$

where a_{ns} is the frequency constant of the transverse free vibration of the plate, which is determined by the boundary conditions, the outer diameter a , the inner diameter b and the surface density ρ'_A of the rigid mass [31].

3.2. Simulation of the ring flexure hinge

The static and dynamic simulation analysis of the ring flexure hinge of the low-frequency vibration system of the device is carried out by ANSYS workbench, and the axial stiffness of the device is compared with the theoretical design. The axial stiffness of the ring flexure hinge is compared with that of the theoretical design. The strength of the ring flexure hinge is checked and the limit speed of the device is determined.

Considering the overall size of the device and the processing factors of the annular flexure hinge, the outer diameter $a=33.5$ mm, the inner diameter $b=17.5$ mm, and the thickness $h=0.6$ mm of the ring flexure hinge are determined. The material is 65Mn spring steel with elastic modulus $E=1.986 \times 10^{11}$ Pa, Poisson's ratio $\nu=0.288$ and density $\rho=7.81$ g/cm³.

Firstly, the finite element model is established according to the size of ring flexure hinge. According to Eq. (12), when the transverse shear force $Q_0=1762.6$ N/m is applied to the outer ring of the thin ring plate, the axial displacement w can be calculated as 200 μ m, which meets the design requirements. The boundary conditions of the simulation are consistent with the theoretical boundary conditions that is the inner ring of the ring plate is fixed, and the outer ring of the thin ring plate is subject to the transverse shear force of 1762.6 N/m. In addition, the outer ring is restrained from rotation. The results of the static simulation

of the ring flexure hinge are shown in Fig. 6.

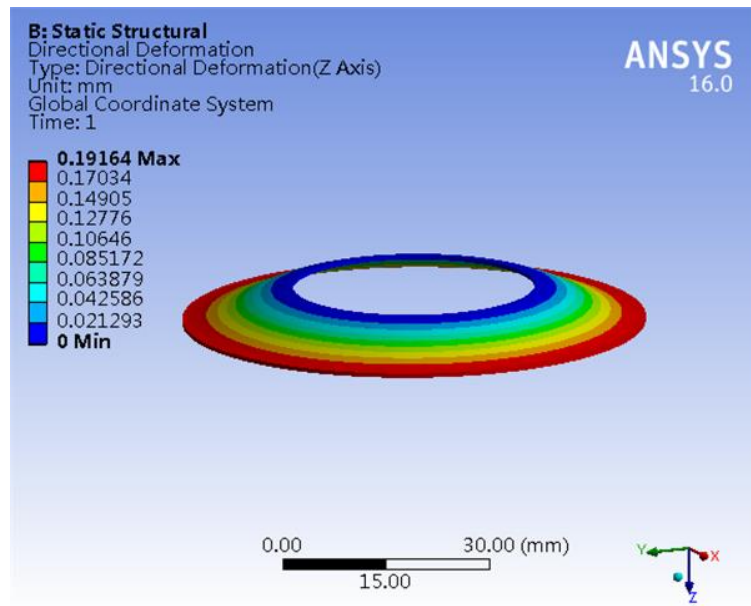


Fig. 6 Static simulation of ring thin plate

From Fig. 6, it is easy to know that the maximum axial displacement w was 191.64 μm . According to Eq. (13), it can be calculated that the axial stiffness K is 1.935 $\text{N}/\mu\text{m}$, which differs 4.37% from the theoretical value of 1.854 $\text{N}/\mu\text{m}$.

If there are no chamfers in the inner ring and outer ring joints of ring flexure hinge, singular stress points will appear in the strength analysis (as the mesh becomes more and more dense, the stress increases infinitely). Therefore, chamfers should be added to the inner and outer ring joints of ring flexure hinge in the strength analysis. Adding chamfering to the inner and outer ring joints increases the average thickness of the ring thin plate, which will affect its stiffness. In actual processing, chamfering is often used to reduce stress concentration, so it is necessary to establish a finite element model with chamfering for stiffness and strength simulation analysis.

A finite element model of the connecting rod with a chamfer radius of 1 mm at the inner and outer ring joints was established, and the stiffness and strength were analyzed. The upper part of the connecting rod is fixed, and the downward uniform transverse shear force is 1.7626 N/mm acting on the outer ring connection of the thin ring plate. The results of the axial displacement of the thick ring of the connecting rod are shown in Fig. 7.

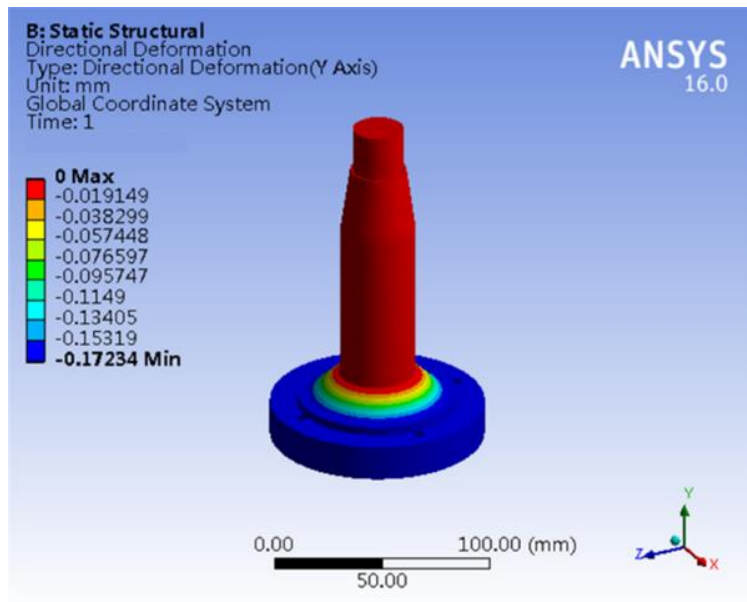


Fig. 7 Static simulation of ring flexure hinge with chamfers

It is evident that the chamfers have a great influence on the axial stiffness of the ring flexure hinge. The simulation results show that the axial stiffness K of the ring flexure hinge is $2.151 \text{ N}/\mu\text{m}$, which differs 11.2% from that of the non-chamfering flexure hinge.

Next, the strength of the ring flexure hinge with chamfers is analyzed. The top of the connecting rod is fixed, and the thick ring is loaded with the downward displacement load of $200 \mu\text{m}$. The results are shown in Fig. 8. It is found that the maximum stress occurs at the joint between the ring thin plate and the interior, which is 355.16 MPa . The yield strength of 65Mn spring steel after heat treatment is 785 MPa and the safety factor $s=785/355.16=2.21>1$. Therefore, the strength condition is satisfied when the amplitude is $100 \mu\text{m}$.

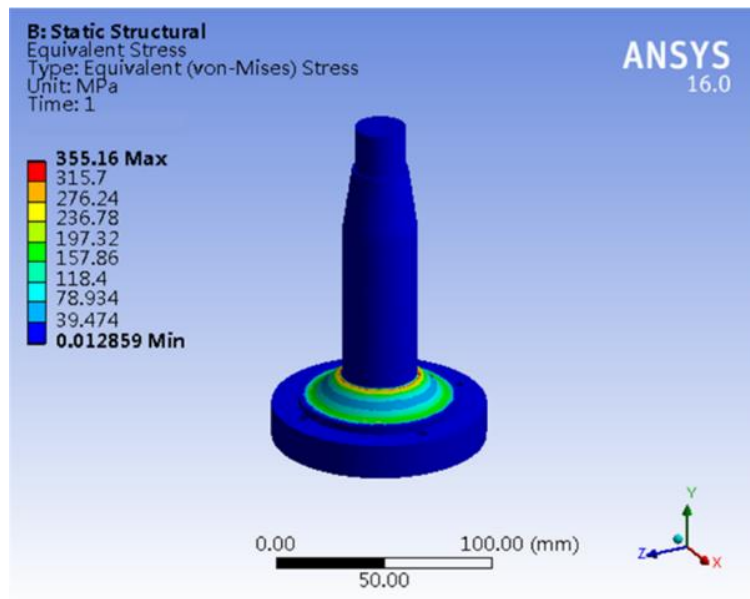


Fig. 8 Strength analysis of ring flexure hinge with chamfers

Then, the dynamic simulation analysis is carried out. First, the modal analysis of the ring flexure hinge with chamfers is carried out. The previous four natural frequencies are obtained as shown in Table 1 and the first four modes are shown in Fig. 9.

Table 1

Previous four natural frequencies

mode	1	2	3	4
Frequency (Hz)	224.96	225.21	390.47	1655.9

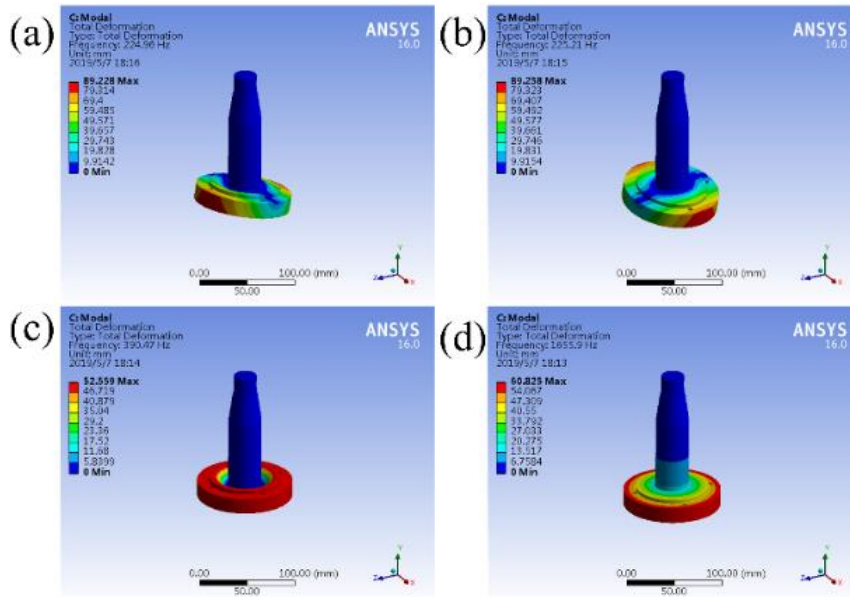


Fig. 9 Previous four modes. (a) First mode; (b) Second order mode; (c) Third order mode; (d) Fourth order mode.

Next, the harmonic response is analyzed. The frequency range is set to 0-500 Hz. The top of the connecting rod is fixed, and the outer ring of the thin ring plate is subject to the downward transverse shear force of 1762.6 N/m. The results are shown in Fig. 10.

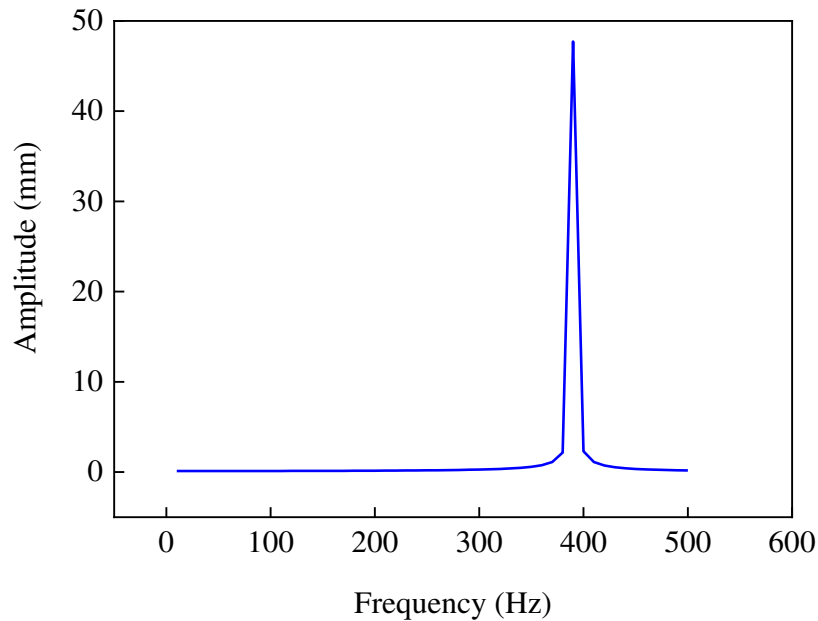


Fig. 10 Harmonic response analysis curve

The resonance frequency is about 390 Hz, so the vibration frequency of the low-frequency vibration system of the device

can't be higher than 390 Hz. When the frequency-to-rotation ratio of low frequency is 5, the spindle speed of the machine tool can't exceed 4680 r/min. Therefore, in the actual processing process, the spindle speed of machine tool is limited.

3.3 Test of the ring flexure hinge

The test of low-frequency structure is mainly to verify the axial stiffness of ring flexure hinge. The connecting rod is machined according to the designed size, and the axial static stiffness of the connecting rod is tested by using the SANS-CMT5205-200 microcomputer-controlled electronic universal testing machine, as shown in Fig. 11.

The axial force-z displacement curve of the ring flexure hinge is obtained as shown in Fig. 12. It can be found that the axial displacement of the connecting rod is approximately proportional to the applied axial force, and its axial stiffness is calculated to be $1.82 \text{ N}/\mu\text{m}$.

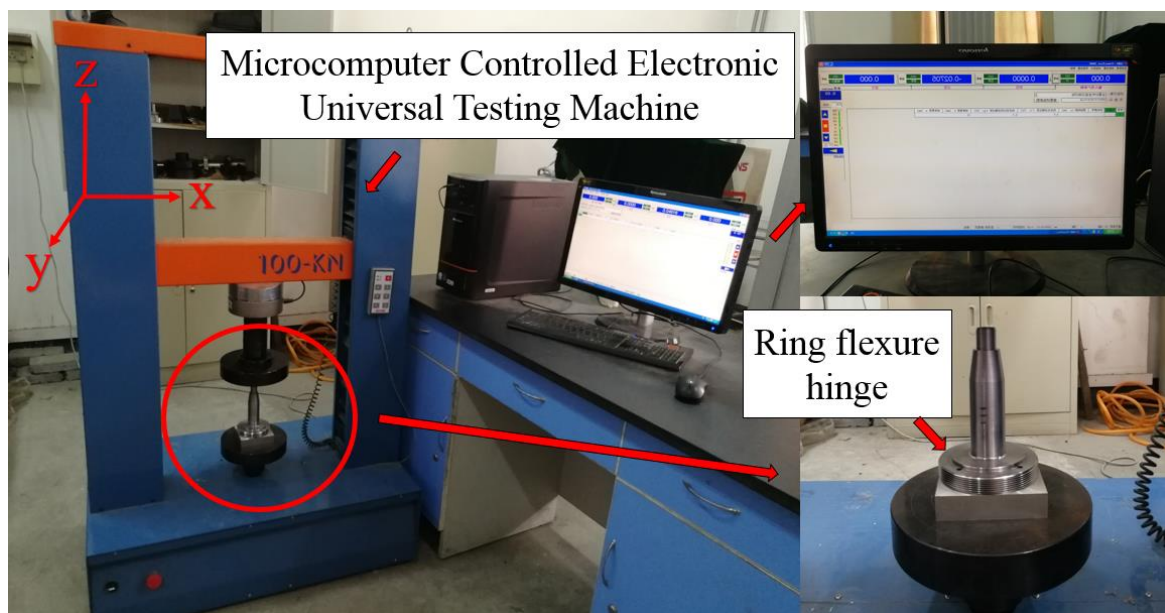


Fig. 11 Compression test site

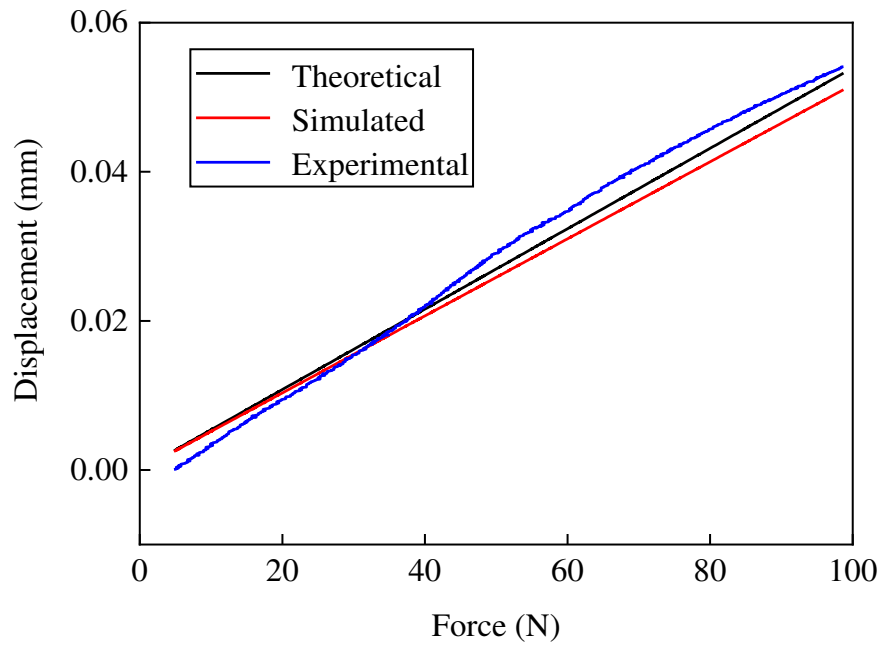


Fig. 12 Force-displacement curve

By comparing the theoretical and experimental stiffness, the difference between the experimental and theoretical values is 1.84%, which verifies the correctness of the theoretical calculation. The difference between the experimental value and the simulation value of the ring flexure hinge with chamfers is large, which is 15.39%. The reason may be that the thickness h of ring flexure hinge has a great influence on its axial stiffness. It is unavoidable that there are machining errors in processing. Also in compression tests, there may be some test errors. Meanwhile, the uniformity of heat treatment and creep characteristics of materials may affect their axial stiffness.

4 Performance test of the LfvAD device

4.1 Vibration performance test

The LfvAD device and its vibration performance test site under no-load condition are shown in Fig. 13. The device can be directly installed on VMC-850E of vertical machining center (speed range 50-6500 r/min, positioning accuracy ± 0.0075 mm, tool handle specification BT40). The KEYENCE LK-G10 non-contact laser measuring system (Sampling frequency 6.5 kHz) is

used to measure the axial low-frequency vibration of the output terminal of the device without load. Because there is no reference plane perpendicular to the axis of twist drill in the cutting part of twist drill, the carbide twist drill is replaced with cylindrical rod for measurement.

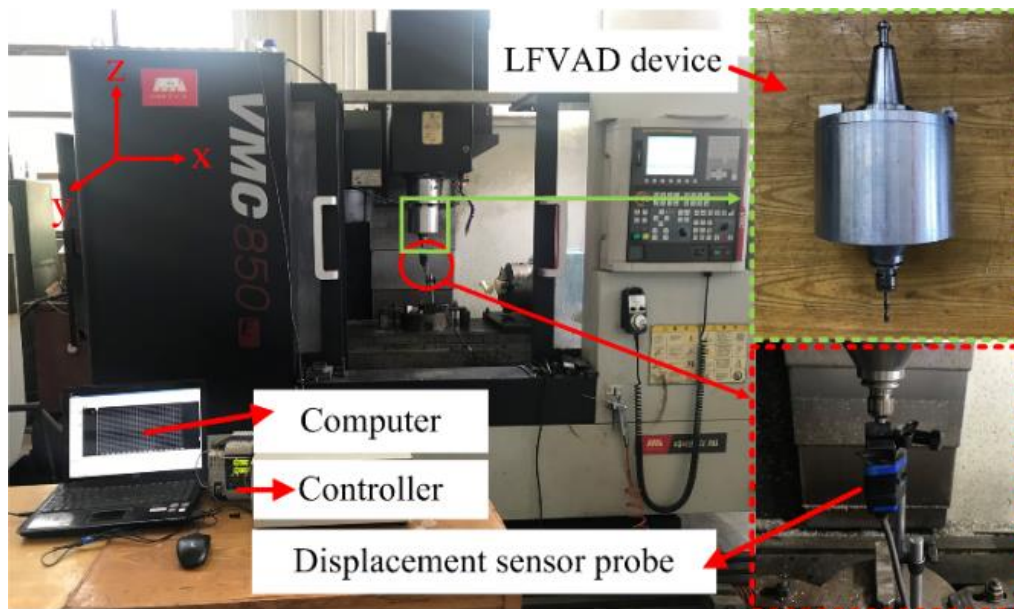


Fig. 13 Vibration performance test site of the device

When the phase difference between the upper and lower sinusoidal end cam is adjusted to 30° by rotating the locknut, the maximum low-frequency amplitude can be calculated as $17.36 \mu\text{m}$ from Eq. (1) in the third section. When the spindle speed of the machine tool is set to 540 r/min , the low-frequency axial vibration results of the tool are shown in Fig. 14. The overall average low-frequency amplitude is about $15 \mu\text{m}$, which is lower than the theoretical calculation amplitude, and the deviation is within the acceptable range. It can be seen from Fig. 14(b) that the frequency of low-frequency vibration is 50 Hz , which is consistent with the frequency-to-rotation ratio of the device at this spindle speed. It is demonstrated that the low-frequency vibration of the device under no-load condition is stable, which meets the design requirements.

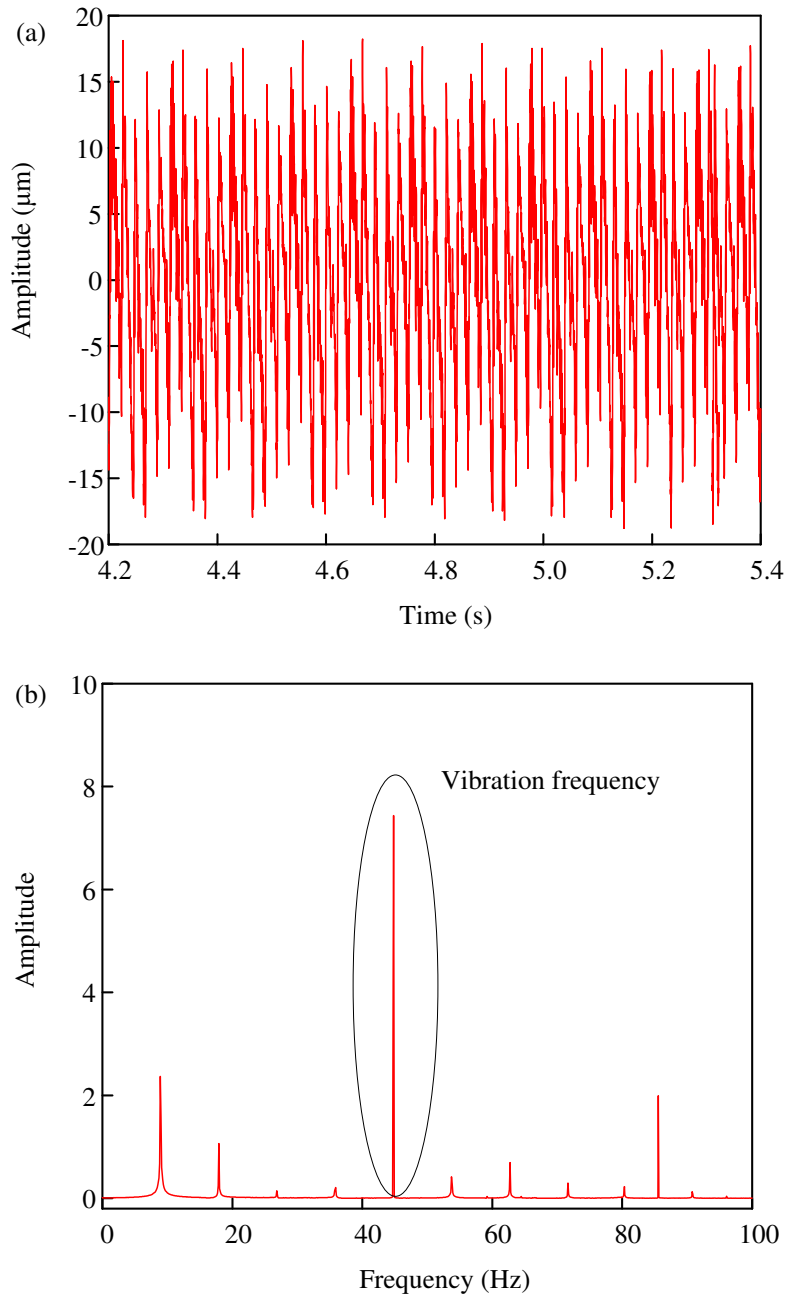


Fig. 14 Low-frequency vibration test results: (a) time domain, (b) frequency domain

4.2 Drilling performance test

The drilling performance test of the LFVAD device was carried out with two cases of typical drilling operation. The first one is titanium alloy drilling and the second one is CFRP / titanium alloy laminated structure drilling, as shown in Fig. 15 (a) and (b).

4.2.1 Titanium alloy drilling

In this experiment, the carbide twist drill (YG6X) with the diameter of 5 mm, point angle 135° and helix angle 30° was used to drill titanium alloy (Ti-6Al-4V, 300 mm \times 150 mm \times 10 mm), as shown in Fig.15 (a).

The material properties of Ti-6Al-4V are showed in Table 2 and the drilling conditions are presented in Table 3. In the drilling process, three-way piezoelectric ceramic dynamometer (KISTLER 9257B) was used to collect the thrust force, and the sampling frequency was 20 kHz.

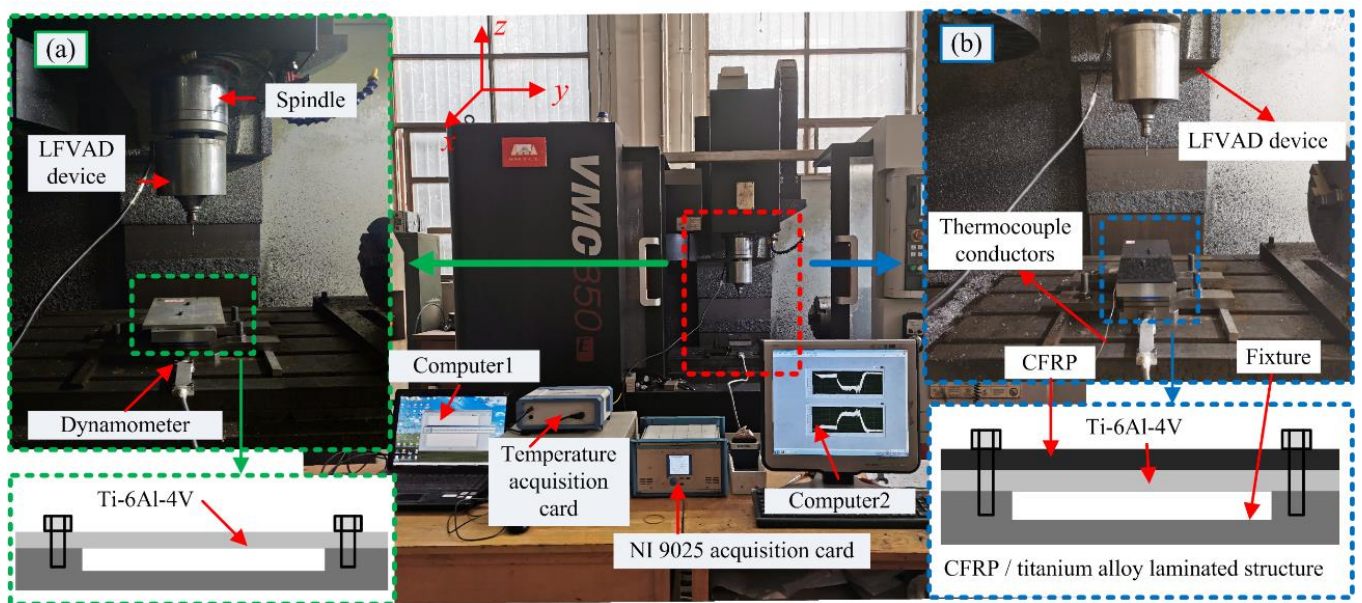


Fig. 15 Drilling performance test

Table 2

Material properties of Ti-6Al-4V

Properties	Value
Density (g/cm ³)	4.4
Elastic modulus (GPa)	109
Tensile strength (MPa)	950

Poisson's ratio	0.34
Elongation (%)	8
Hardness(HV)	360
Thermal conductivity(W/ (m·°C))	7.5

Table 3

Drilling conditions of titanium alloy drilling

Variable	level
Spindle speed /(r/min)	400
Feed rate /(mm/r)	0.05
Amplitude /(μm)	0, 10, 20, 30
Frequency /(Hz)	33.33

Figure 16 shows the time and frequency domain signals of thrust force during drilling process when the amplitude is 20 μm. LFVAD presents intermittent cutting process, and increases the instantaneous impact force in the cutting process. It is noticed from Fig. 16 (b) that the frequency of low-frequency vibration is still stable under load conditions, which further proves that the ring flexure hinge is feasible as the elastic recovery mechanism of the device.

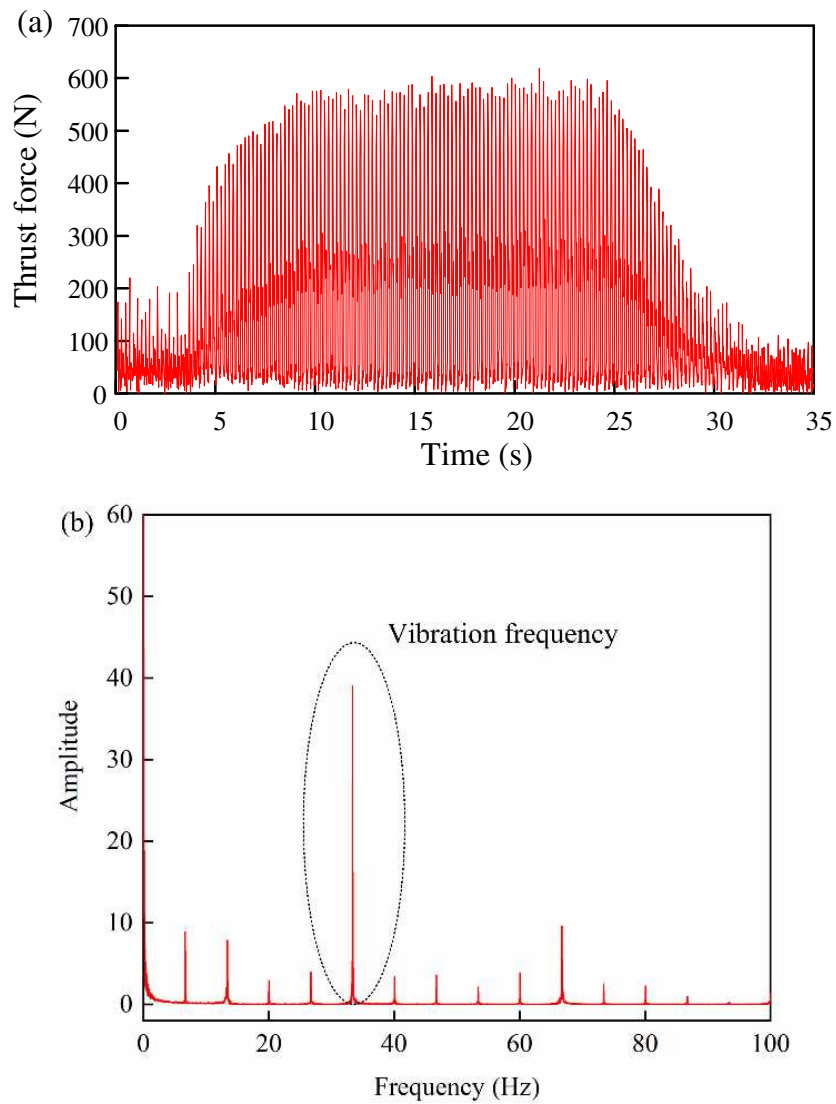


Fig. 16 Drilling performance test

The chip morphology reflects the movement path of the tool to some extent. The chip morphology of titanium alloy under different amplitudes were analyzed and compared. Figure 17 shows the chips morphology of titanium alloy with different amplitudes under the same processing parameters.

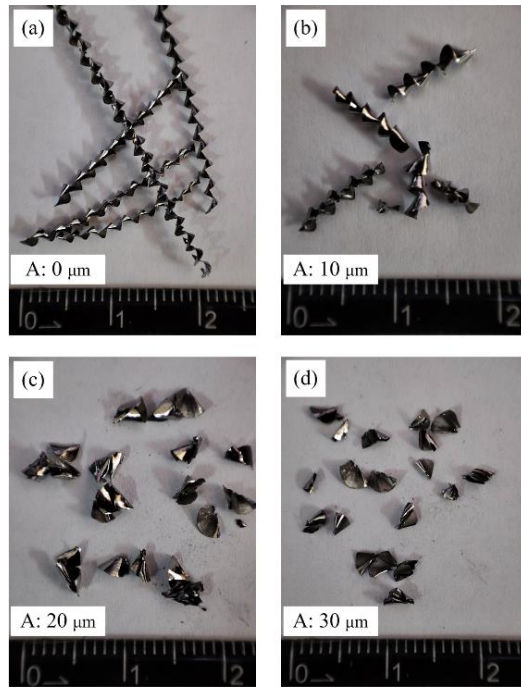


Fig. 17 Chip morphology

As shown in Fig. 17 (a), when the amplitude of the low-frequency vibration is $0 \mu\text{m}$, it is conventional drilling (CD). The CD produces continuous conical helix type chip with long length. It is difficult to break the titanium alloy chips because of the constant cutting thickness in the CD process.

Fig. 17 (b) shows the chip morphology of titanium alloy with amplitude of $10 \mu\text{m}$. According to Eq. (2), when the amplitude A is $10 \mu\text{m}$ and the feed rate f_r is 0.05 mm/r , the theoretical chip breaking condition is not satisfied ($4A/f_r < 1$). Therefore, what is generated is still conical helix type chip with short length.

Broken titanium alloy chips are generated when the amplitude is $20 \mu\text{m}$ and $30 \mu\text{m}$, shown in Fig. 17 (c) and (d). Because the amplitude and feed rate meet the theoretical chip breaking conditions ($4A/f_r > 1$), the tool and workpiece can be separated and contacted periodically in the drilling process, resulting in broken chips.

Therefore, the chip breaking effect can be achieved by selecting appropriate processing parameters and vibration parameters. The drilling performance of the designed LFVAD device meets the actual processing requirements.

4.2.2 CFRP / titanium alloy laminated structure drilling

In this experiment, the carbide twist drill (YG6X) with the same structural parameters was used to drill CFRP (T700-12K/AG80, 32 lays of unidirectional laying, 300 mm×120 mm×5 mm) / titanium alloy (Ti-6Al-4V, 300 mm×210 mm×5 mm) laminated structure. K-type thermocouple was used to detect the temperature 0.5 mm away from the hole wall of titanium alloy in the process of drilling titanium alloy layer, and the measurement data was read by the fast response thermocouple acquisition instrument (HR-USB-T008), as shown in Fig.15 (b). Finally, the machining quality of CFRP was observed by using the super depth of field microscope and scanning electron microscope.

The material properties of CFRP are shown in Table 4 and the drilling conditions of CFRP/ titanium alloy drilling are presented in Table 5.

Table 4

Material properties of T700-12K/AG80 CFRP

Properties	Value
Density/ (g/cm ³)	1.55
Fiber volume fraction/ %	60%
Transverse modulus /(GPa)	40
Longitudinal modulus /(GPa)	230
Tensile strength/(MPa)	4900
Glass transition temperature/(°C)	≥230

Table 5

Drilling conditions of CFRP / titanium alloy laminated structure drilling

Variable	Level
----------	-------

Spindle speed /(r/min)	400
Feed rate /(mm/r)	0.03, 0.04, 0.05, 0.06
Amplitude /(μm)	0, 20
Frequency /(Hz)	33.33

Figure 18 presents the measured temperature curves during drilling at feed rates of 0.03 mm/r and 0.06 mm/r. Compared with CD ($A=0 \mu\text{m}$), the maximum temperature of LFVAD with amplitude of $20 \mu\text{m}$ is reduced by about 44%. LFVAD changes the cutting process from continuous cutting to intermittent cutting, which increases the duty cycle of the tool. In addition, the discontinuous titanium alloy chips are efficiently discharged from the hole along the spiral groove, which takes away a large amount of cutting heat.

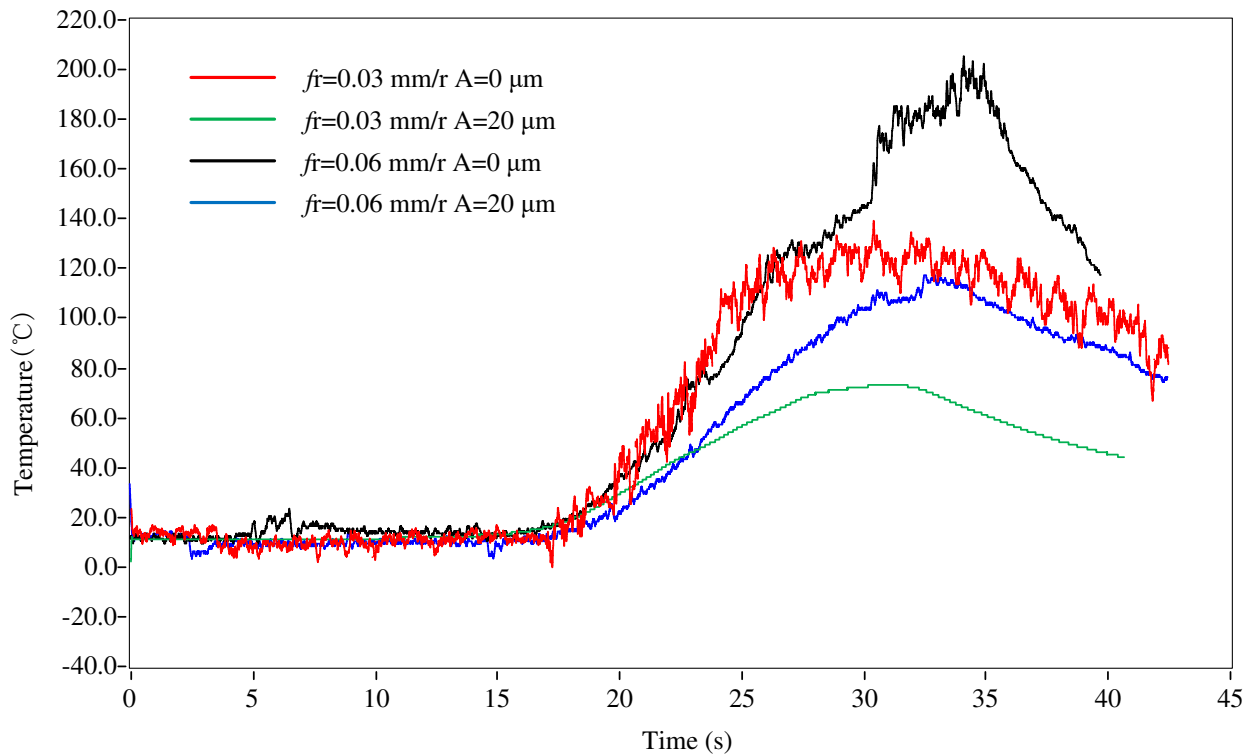


Fig. 18 Temperature of drilling process

In the process of drilling CFRP / titanium alloy laminated structure, the drilling temperature of titanium alloy and the chip morphology of titanium alloy have great influence on the machining quality of CFRP. The delamination factor “ Φ_d ” is evaluated

using Eq. (22):

$$\Phi_d = \frac{S_{\text{actual}} - S_{\text{nominal}}}{S_{\text{nominal}}} \quad (22)$$

where S_{actual} represents the area of a circle that is concentric to the hole and circumscribing the delamination extents, while S_{nominal} is the nominal hole area [32].

Figure 19 shows the observation results of the entrance and exit of the CFRP hole and the SEM morphologies of the drilled CFRP hole walls with the fiber orientation angle at 90° .

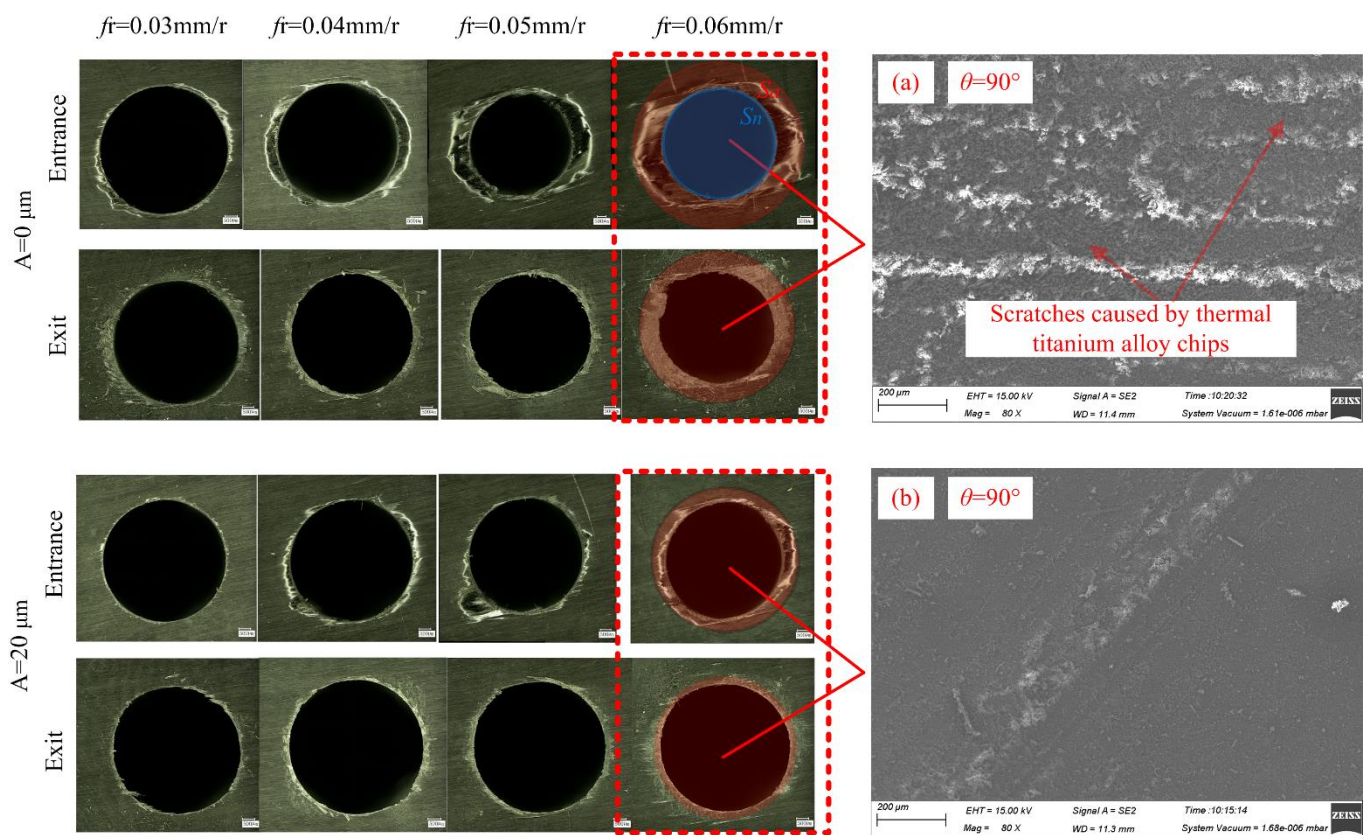


Fig. 19 The entrance and exit morphology of CFRP

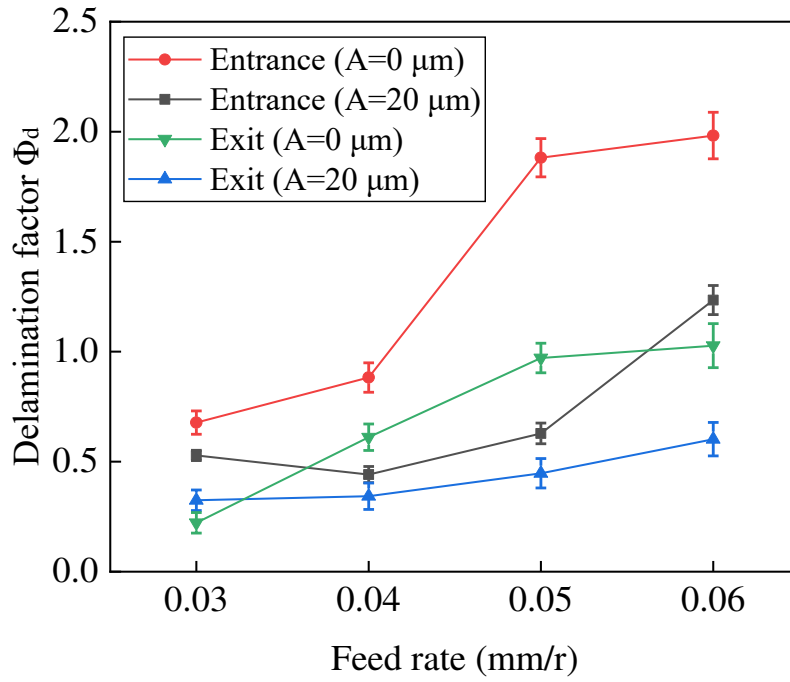


Fig. 20 Delamination factor

In the drilling process of CFRP / titanium alloy laminated structure, the titanium alloy under the CFRP plate plays a good supporting role, which reduces the delamination defects at the CFRP hole exit, resulting in the delamination factor of hole entrance larger than that of hole exit. In addition, compared to CD, the delamination factor of CFRP hole under LFVAD is smaller and increases slower with the increase of feed rate, as shown in Fig.20. The drilling temperature of LFVAD is lower than that of CD. Besides, the intermittent titanium alloy chips can be discharged along the spiral groove efficiently, which reduces the scraping of the chip on the CFRP hole wall, thus significantly reducing the delamination factor of CFRP hole and improving the quality of the CFRP hole wall.

5 Conclusions

In this paper, a novel ring flexure hinge is used as elastic recovery mechanism to develop the low-frequency vibration-assisted drilling device. The vibration performance of the device is tested under no-load condition, and the actual drilling test verified the drilling performance. The results are summarized as follows:

1. The simulation and test of ring flexure hinge verified the correctness of the theoretical design. The ring flexure hinge has good linear elasticity and the structural parameters determine its stiffness, which affects the limit speed of the device.

2. The thickness h of the ring flexure hinge has a great influence on its deflection. The deflection increases with the increase of the thickness, and the influence degree of the thickness on the deflection gradually decreases with the increase of the thickness. When the inner diameter b is determined, the deflection increases with the increase of the outer diameter a .

3. Through the performance test, the LFVAD device presents good working stability under no-load and load conditions, which indicates that the device could meet the actual processing requirements and provides guidance for the design of low-frequency vibration-assisted drilling device.

4. The LFVAD device could realize axial low-frequency vibration of the tool with constant frequency-to-rotation ratio and amplitude stepless adjustment. The actual drilling test shows that LFVAD significantly reduces the drilling temperature and produces discontinuous titanium alloy chips, which restrains the secondary damage of CFRP and improves the machining quality.

Declarations

Ethical Approval

Not applicable

Consent to Participate

Not applicable

Consent to Publish

Not applicable

Authors Contributions

Feng Jiao: Conceptualization, Supervision, Methodology, Funding acquisition, Writing-review & editing. **Yuanxiao Li:** Conceptualization, Methodology, Software, Writing-original draft. **Dong Wang:** Investigation, Software. **Jinglin Tong:** Investigation, Resources. **Ying Niu:** Software, Supervision.

Funding

This work was supported by the National Natural Science Foundation of China (Grant No. 51675164) and Natural Science Foundation of Henan (No.202300410172).

Competing Interests

The authors declare that they have no known competing financial interests or personal relationships that could have appeared to influence the work reported in this paper.

Availability of data and materials

Not applicable

Code availability

Not applicable

Acknowledgements

The authors acknowledge the National Natural Science Foundation of China (Grant No. 51675164) and Natural Science Foundation of Henan (No.202300410172) for the support of this paper.

References

1. Qiu X, Li P, Li C, Niu Q, Chen A, Ouyang P (2019) New compound drill bit for damage reduction in drilling CFRP.

2. Zhang XS, Chen YJ, Hu JL (2018) Recent advances in the development of aerospace materials." *Progress in Aerospace Sciences* 97: 22–34. <https://doi.org/10.1016/j.paerosci.2018.01.001>
3. Shyha, IS, Soo, SL, Aspinwall, DK, Bradley, S, Perry, R, Harden, P (2011) Hole quality assessment following drilling of metallic-composite stacks. *International Journal of Machine Tools & Manufacture* 51(7-8), 569-578.
<https://doi.org/10.1016/j.ijmachtools.2011.04.007>
4. Park, KH, Beal, A, Kim, D, Kwon, P, Lantrip, J (2011) Tool wear in drilling of composite/titanium stacks using carbide and polycrystalline diamond tools. *Wear* 271(11-12), 2826-2835. <https://doi.org/10.1016/j.wear.2011.05.038>
5. Tashiro, T, Fujiwara, J, Inada, K (2011) Drilling of CFRP/Ti-6Al-4V stacks. *Advanced Materials Research*, 369-374.
<https://doi.org/10.4028/www.scientific.net/AMR.325.369>.
6. Pujana J, Rivero A, Celaya A, López de Lacalle LN (2009) Analysis of ultrasonic-assisted drilling of Ti-6Al-4V. *International Journal of Machine Tools and Manufacture* 49 (6), 500-508.
<https://doi.org/10.1016/j.ijmachtools.2008.12.014>
7. Pecat O, Paulsen T, Katthöfer P, and Brinksmeier E (2016) Vibration Assisted Drilling of Aerospace Materials. SAE Technical Paper 2016-01-2136, 2016, <https://doi.org/10.4271/2016-01-2136>.
8. Dong S, Liao WH, Zheng K, Liu JS, Feng JD (2019) Investigation on exit burr in robotic rotary ultrasonic drilling of CFRP/aluminum stacks. *International Journal of Mechanical Sciences* 151: 868-876.
<https://doi.org/10.1016/j.ijmecsci.2018.12.039>
9. Sanda A, Arriola I, Garcia Navas V, Bengoetxea I, Gonzalo O (2016) Ultrasonically assisted drilling of carbon fibre reinforced plastics and Ti6Al4V. *Journal of Manufacturing Processes* 22: 169–176.
<https://doi.org/10.1016/j.jmapro.2016.03.003>

-
10. Peace Y Onawumi, Anish Roy, Vadim V Silberschmidt , Eleanor Merson (2018) Ultrasonically assisted drilling of aerospace CFRP/Ti stacks. *Procedia CIRP* 77: 383-386. <https://doi.org/10.1016/j.procir.2018.09.041>
 11. Yan MP, Shao H (2011) Analysis of Temperature and Wear of Tool of Ultrasonic Vibration Drilling Ti Alloys. *Tool Engineering* 8: 26-30.
 12. Yang ZC, Zhu LD, Zhang GX, Ni CB, Lin B (2020) Review of ultrasonic vibration-assisted machining in advanced materials. *International Journal of Machine Tools and Manufacture* 156: 103594. <https://doi.org/10.1016/j.ijmachtools.2020.103594>
 13. Sylvain L (2012) Major Breakthrough in Multi Material Drilling, Using Low Frequency Axial Vibration Assistance. *SAE International Journal of Materials & Manufacturing* 6 (1): 11-18. <https://doi.org/10.4271/2012-01-1866>
 14. Yang HJ, Ding WF, Chen Y (2019) Drilling force model for forced low frequency vibration assisted drilling of Ti–6Al–4V titanium alloy. *International Journal of Machine Tools and Manufacture* 103438. <https://doi.org/10.1016/j.ijmachtools.2019.103438>
 15. Alonso U, Goirigolzarri B, and Ostra T (2019) Low frequency vibration assisted drilling of PC1000 polycarbonate. *Procedia Manufacturing* 41: 407-414. <https://doi.org/10.1016/j.promfg.2019.09.026>
 16. Yang, HJ, Yan Chen, Y, Xu, JH, Ladonne M, Ding, WF (2020) Chip control analysis in low-frequency vibration-assisted drilling of ti–6al–4v titanium alloys. *International Journal of Precision Engineering and Manufacturing* 21: 565–584. <https://doi.org/10.1007/s12541-019-00286-8>
 17. Lee PA , Kim Y, Kim BH (2015) Effect of low frequency vibration on micro EDM drilling. *International Journal of Precision Engineering & Manufacturing* 16: 2617-2622. <https://doi.org/10.1007/s12541-015-0335-3>
 18. Pecat O, Meyer I (2013) Low Frequency Vibration-assisted Drilling of Aluminium Alloys, *Advanced Materials Research* 769: 131-138. <https://doi.org/10.4028/www.scientific.net/AMR.769.131>
 19. Pecat O, Brinksmeier E (2014) Tool Wear Analyses in Low Frequency Vibration-assisted Drilling of CFRP/Ti6Al4V Stack

-
- Material. *Procedia CIRP* 14(14): 142-147. <https://doi.org/10.1016/j.procir.2014.03.050>
20. Okamura K, Sasahara H, Segawa T, Tsutsumi M (2006) Low-frequency vibration drilling of titanium alloy. *Jsmc International Journal* 49(1): 76-82. <https://doi.org/10.1299/jsmec.49.76>
 21. Hussein R, Sadek A, Elbestawi MA, Attia MH (2018) Low-frequency vibration-assisted drilling of hybrid CFRP/Ti6Al4V stacked material. *The International Journal of Advanced Manufacturing Technology* 98: 2801-2817. <https://doi.org/10.1007/s00170-018-2410-2>
 22. Kumabe J (1985) *The foundation and application of precision vibration cutting*. Machinery Industry Press, Beijing.
 23. Li ZD, Tian JW, Jiao F (2018) Research and Development Progress of Machine Type Low-Frequency Vibration Motion Technology. *Tool Engineering* 52: 7-10.
 24. Ma QY, Ma QH, Wang B (2013) Mechanical Axial Vibration System Design for Deep Holes Drilling. *Machine Design & Research* 4: 94-95.
 25. Laporte S, De Castelbajac C (2012) Major breakthrough in multi material drilling, using low frequency axial vibration assistance. *SAE Int J Mater Manuf* 6:1–12. <https://doi.org/10.4271/2012-01-1866>
 26. Zhang DY, Wang LJ (1998) Investigation of chip in vibration drilling. *International Journal of Machine Tools and Manufacture* 38 (3):165-176. [https://doi.org/10.1016/S0890-6955\(97\)00047-3](https://doi.org/10.1016/S0890-6955(97)00047-3)
 27. Qiu L, Yue X, Xie Z (2019) Design and analysis of Multicavity Flexure Hinge (MCFH) based on three-dimensional continuum topology optimization[J]. *Mechanism & Machine Theory* 139: 21-33. <https://doi.org/10.1016/j.mechmachtheory.04.004>
 28. Zhang X, Xu Q (2018) Design and testing of a new 3-dof spatial flexure parallel micropositioning stage. *International Journal of Precision Engineering & Manufacturing* 19: 109-118. <https://doi.org/10.1007/s12541-018-0013-3>
 29. Hao GB (2017) Determinate Design and Analytical Analysis of a Class of Symmetrical Flexure Guiding Mechanisms for Linear Actuators. *J Mech Design* 139 (1): 012301. <https://doi.org/10.1115/1.4034579>

-
30. Timoshenko S, Woinowsky-Krieger S (1987) Theory of Plates and Shells. McGraw-Hill Book Company, New York.
 31. Qu WD (1992) Mechanical vibration manual. Mechanical industry press.
 32. Karnik SR , Gaitonde VN, Rubio JC, Correia AE, Davim JP (2008) Delamination analysis in high speed drilling of carbon fiber reinforced plastics (cfrp) using artificial neural network model. Materials and Design 29(9): 1768-1776.

<https://doi.org/10.1016/j.matdes.2008.03.014>

Figures

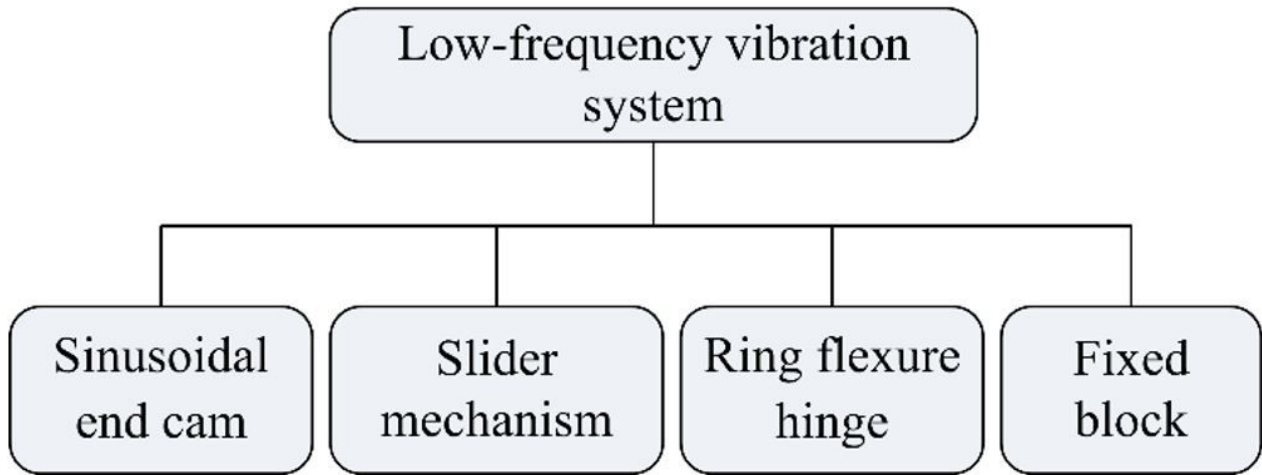


Figure 1

The low-frequency vibration system composition

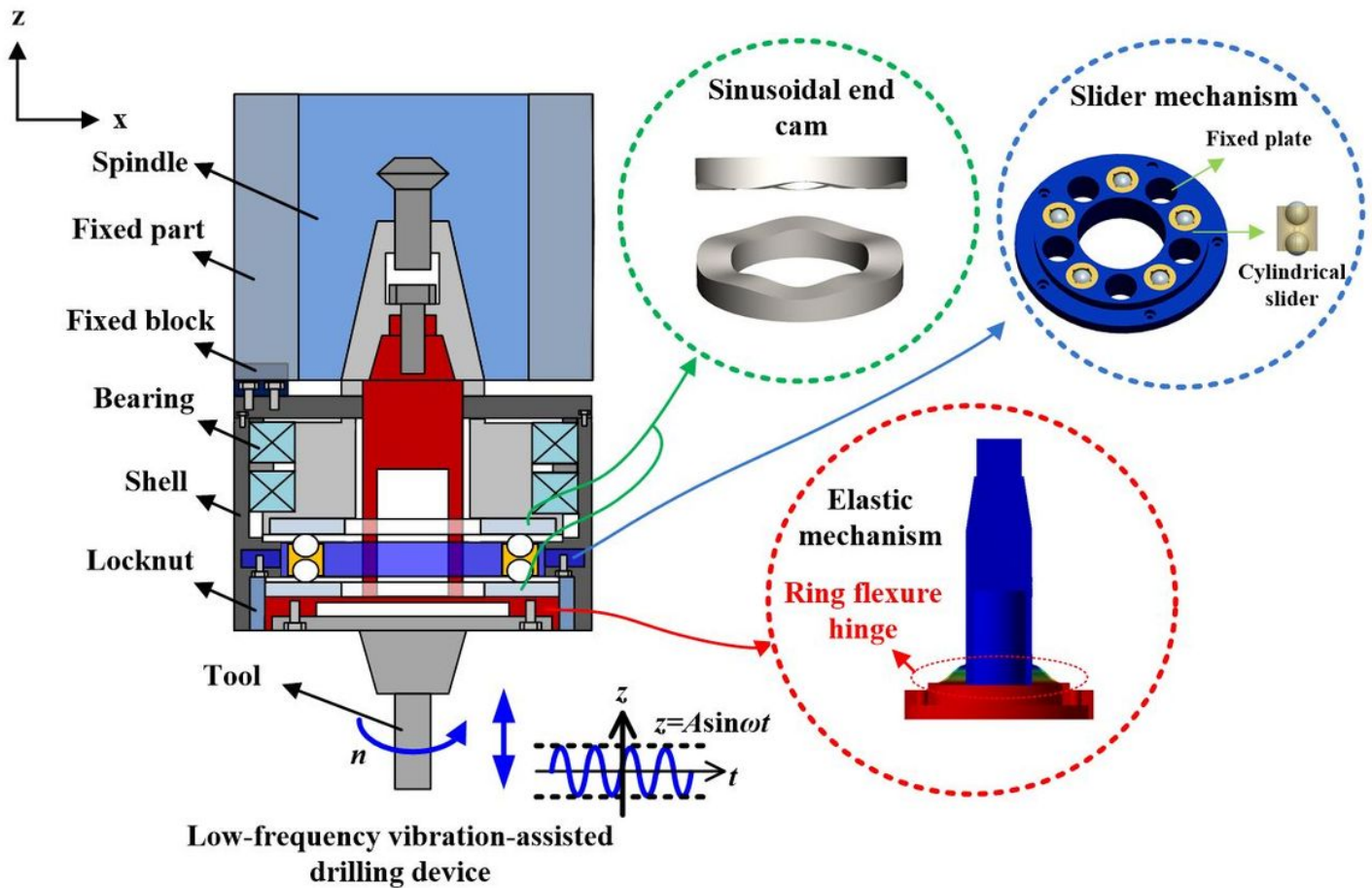


Figure 2

The schematic diagram of the LFVAD device

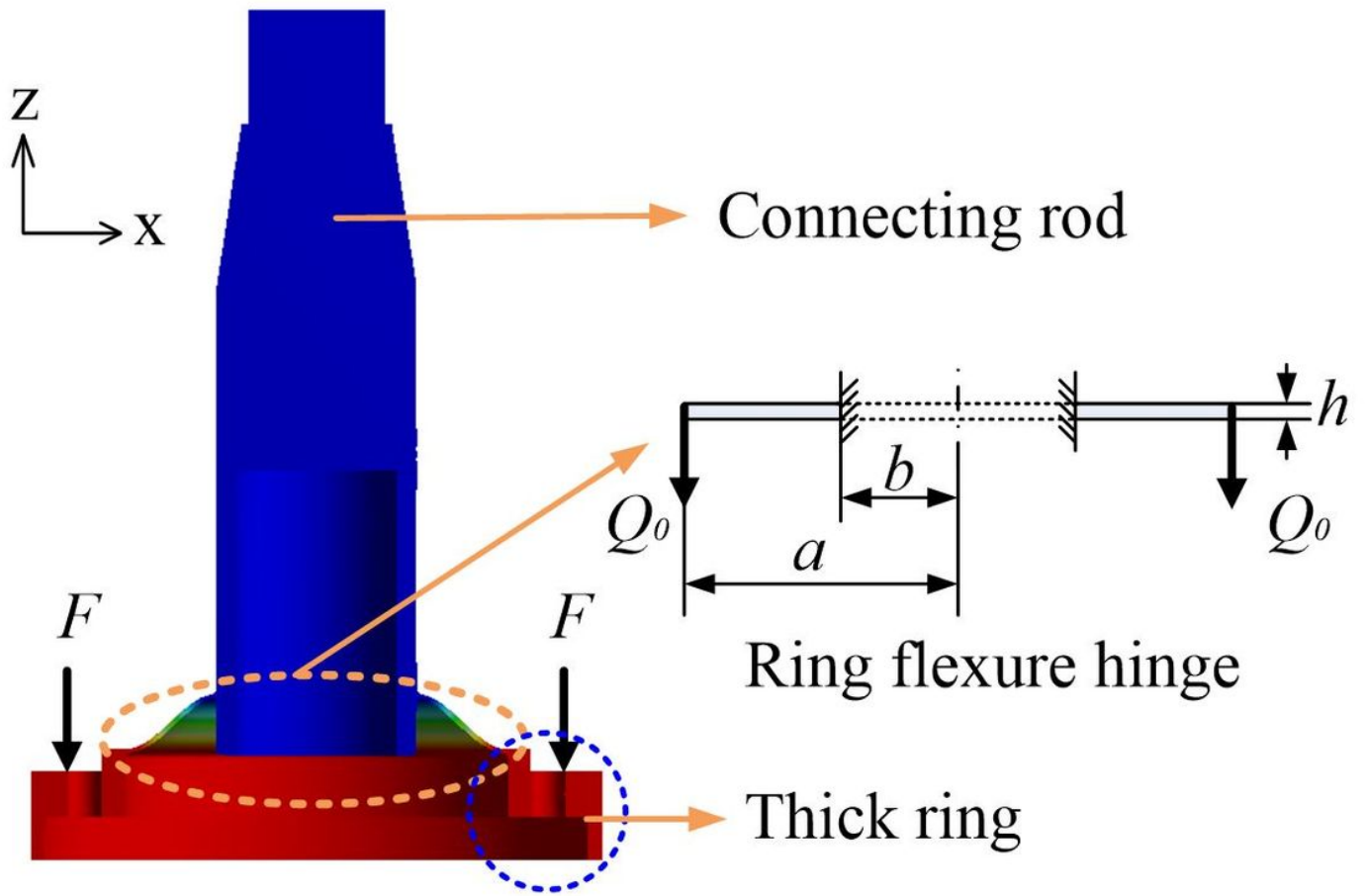


Figure 3

The section of elastic recovery mechanism

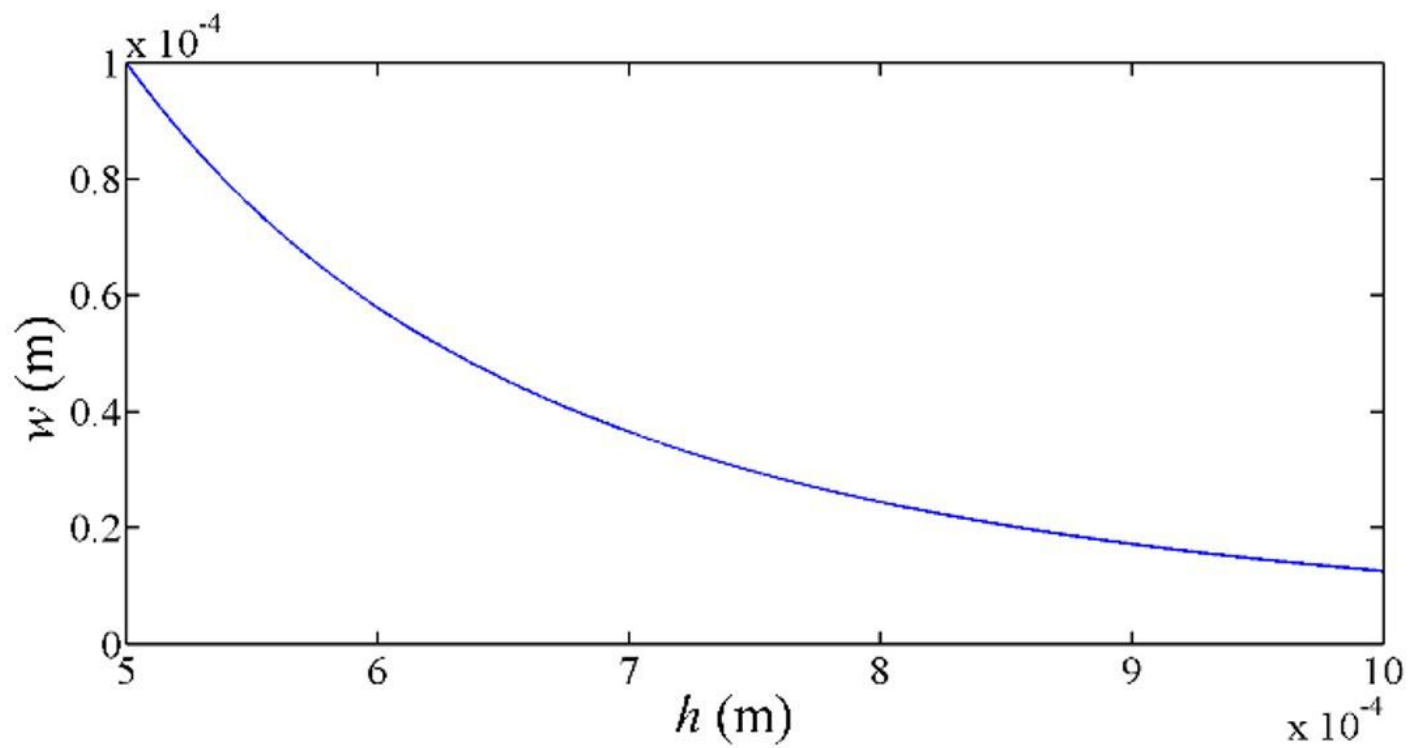


Figure 4

Influence of thickness h

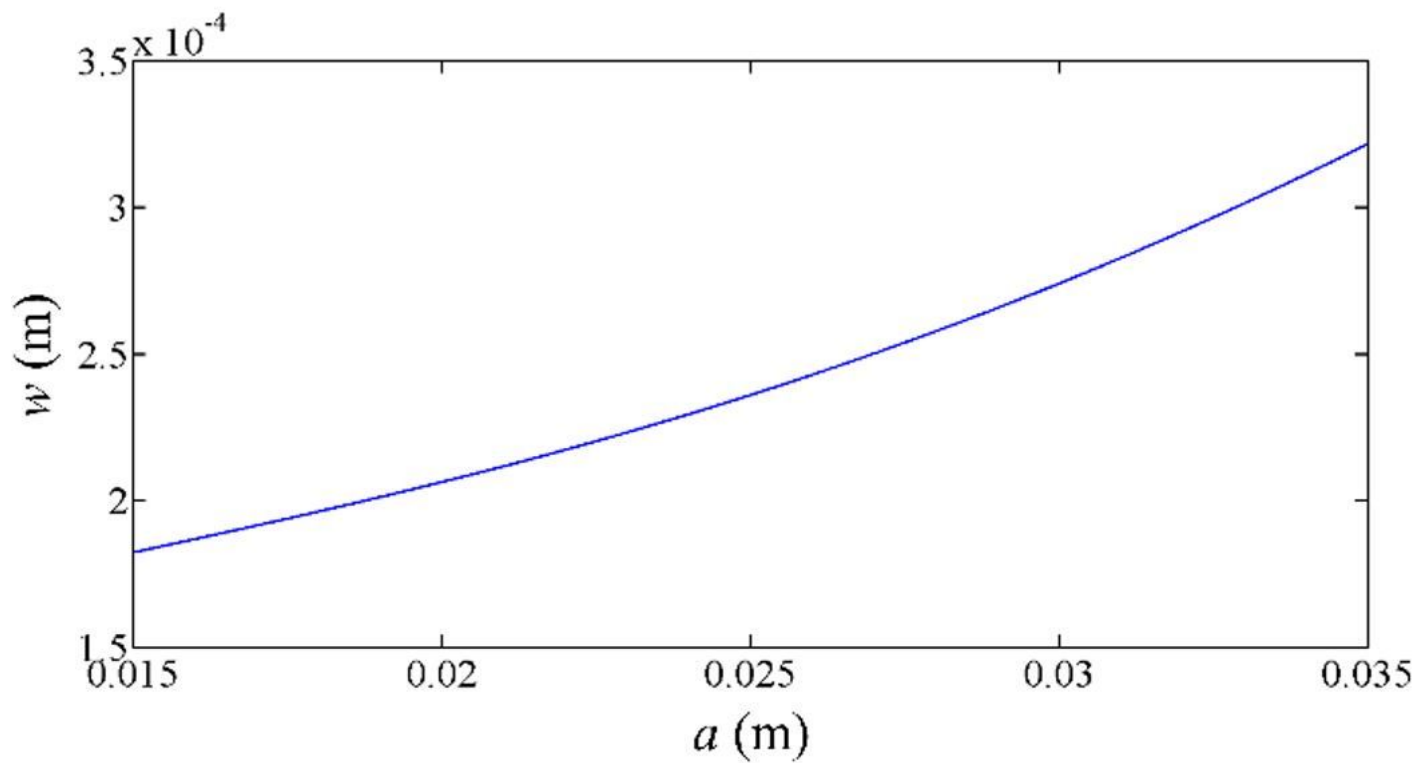


Figure 5

Influence of outer diameter a

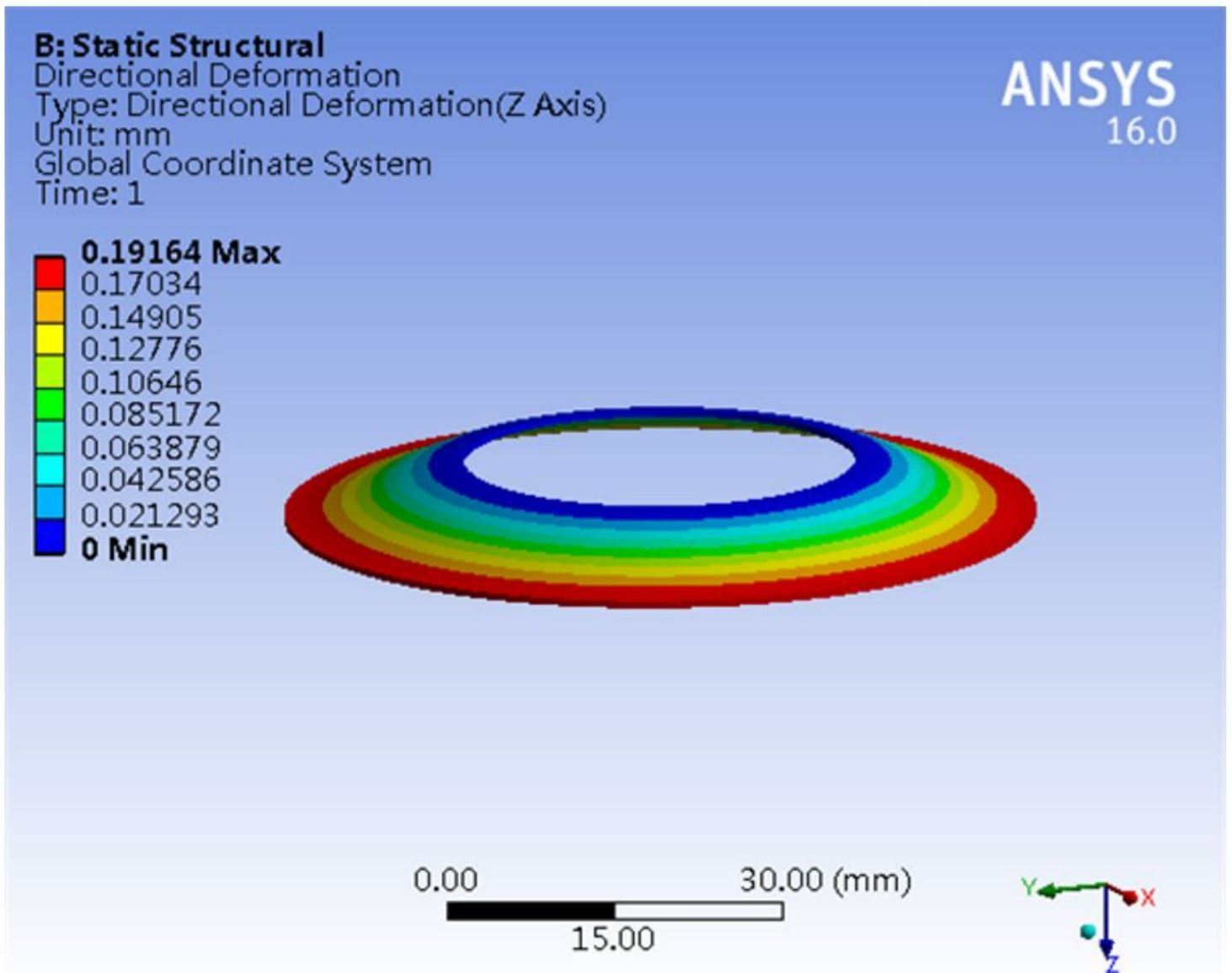


Figure 6

Static simulation of ring thin plate

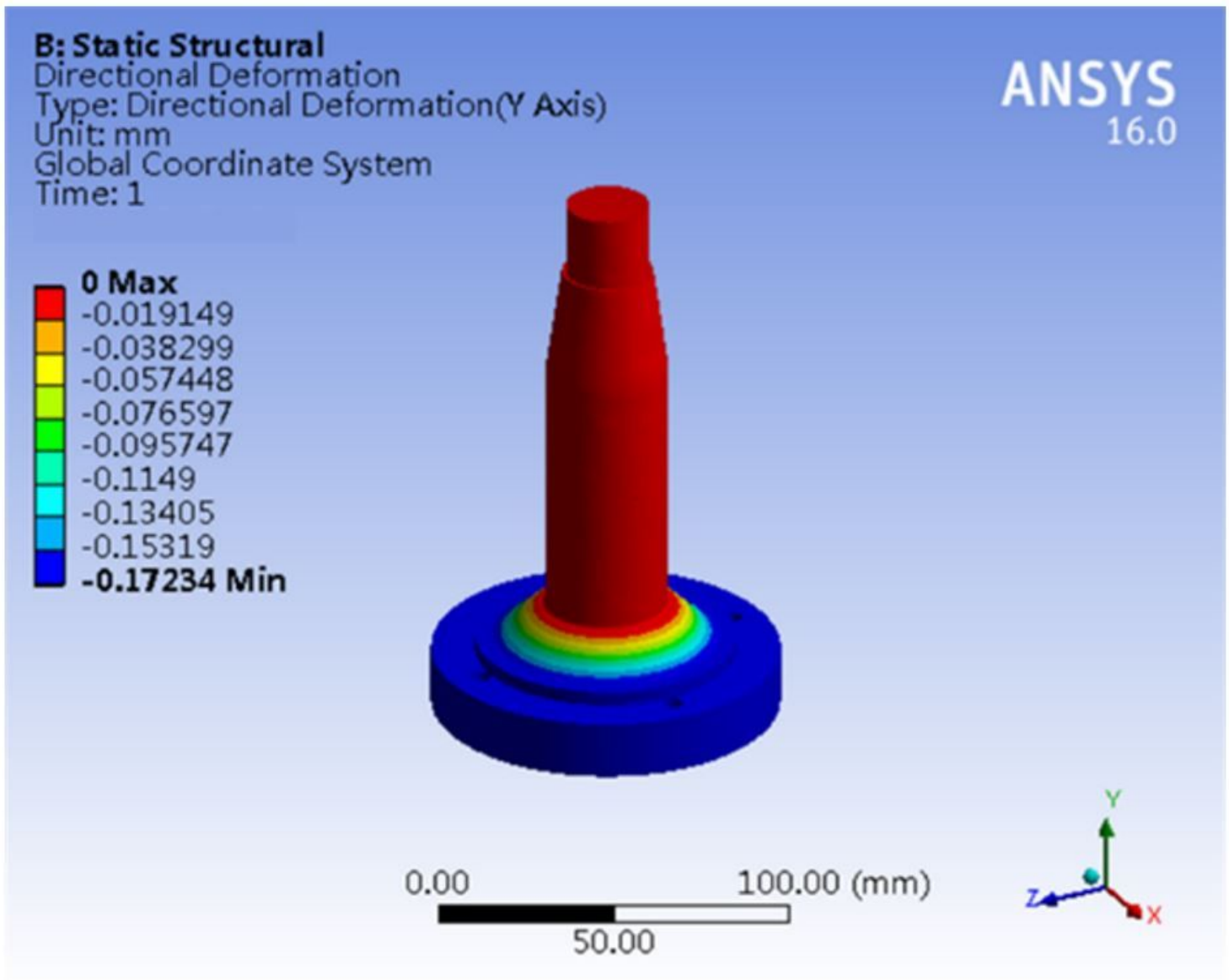


Figure 7

Static simulation of ring flexure hinge with chamfers

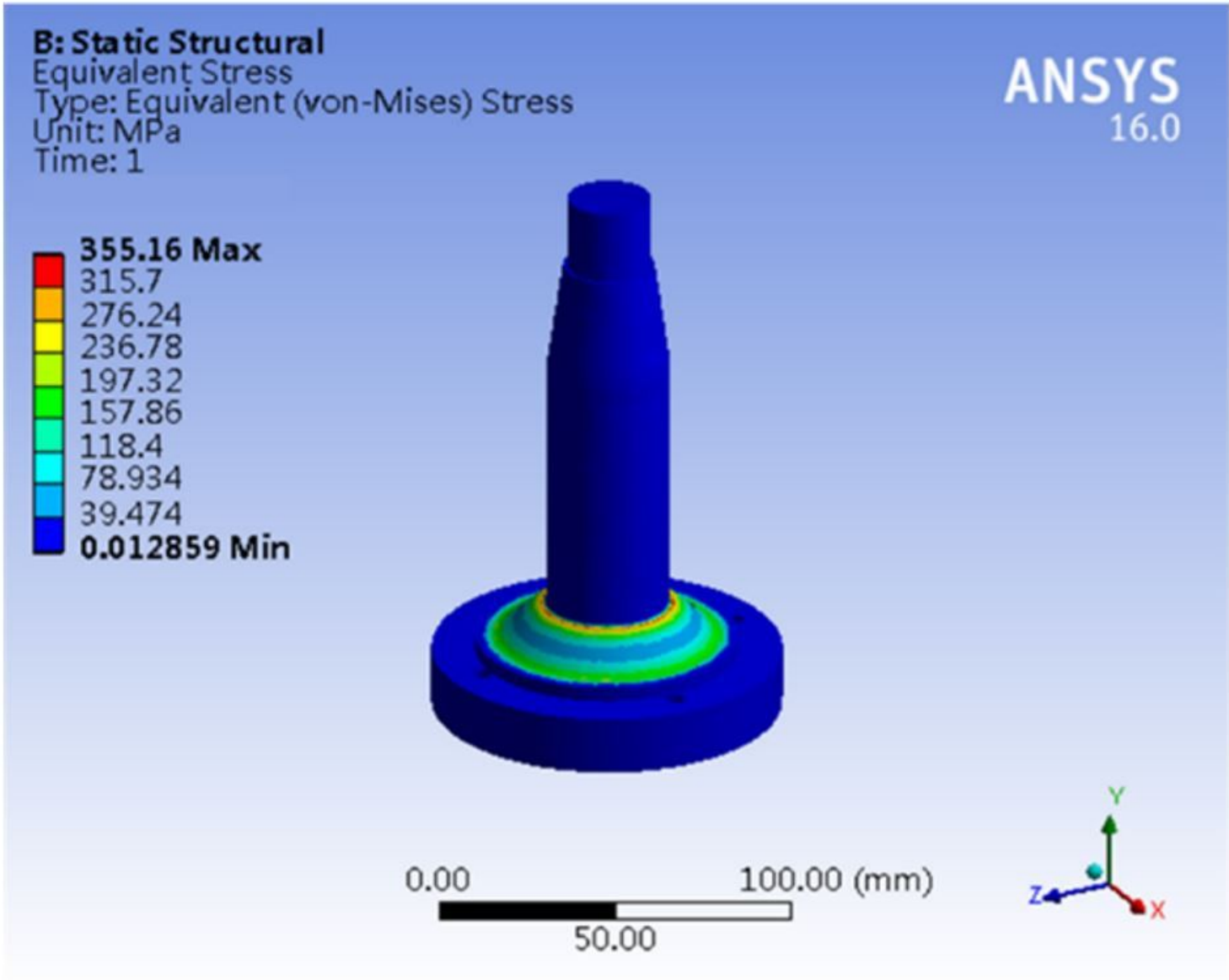


Figure 8

Strength analysis of ring flexure hinge with chamfers

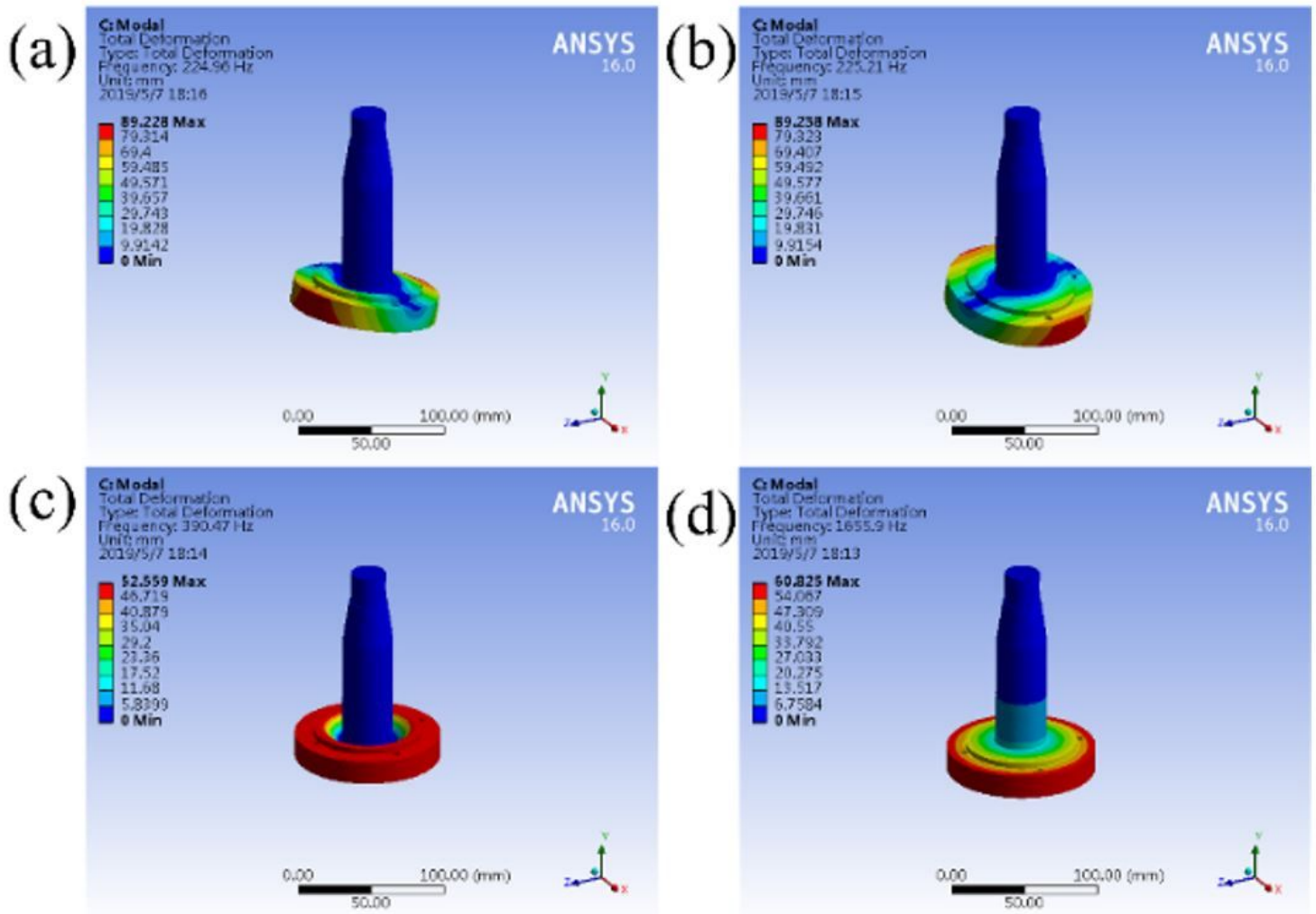


Figure 9

Previous four modes. (a) First mode; (b) Second order mode; (c) Third order mode; (d) Fourth order mode.

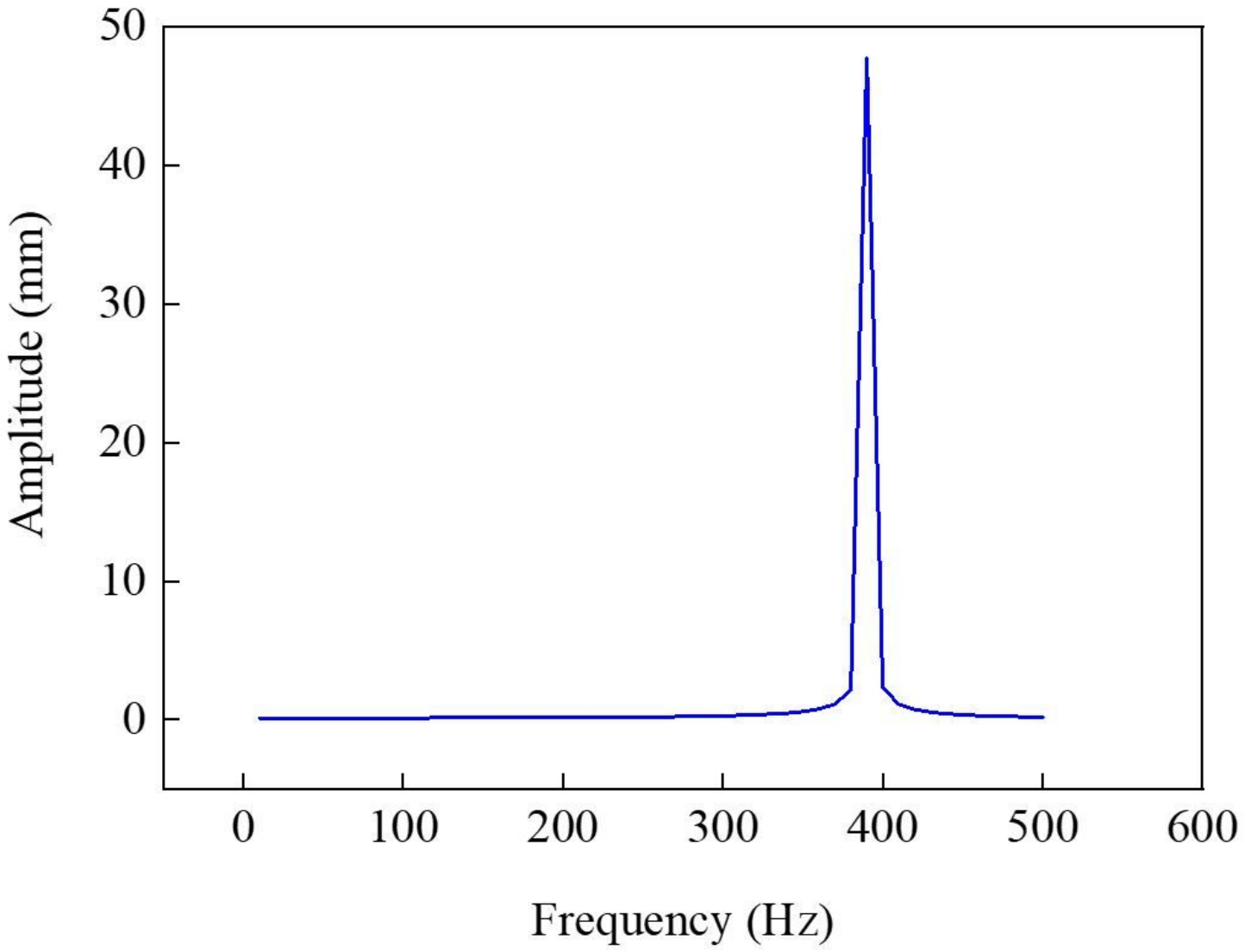


Figure 10

Harmonic response analysis curve

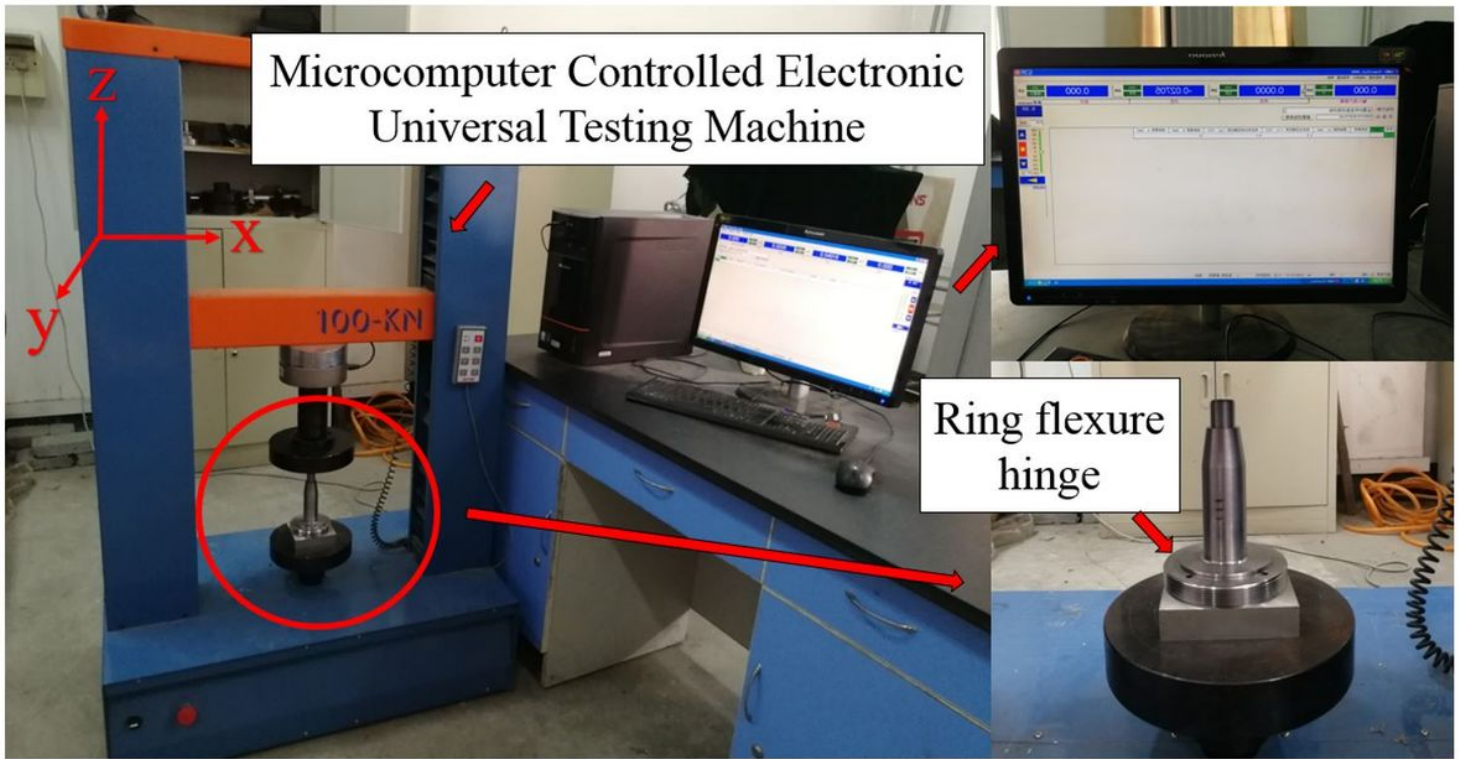


Figure 11

Compression test site

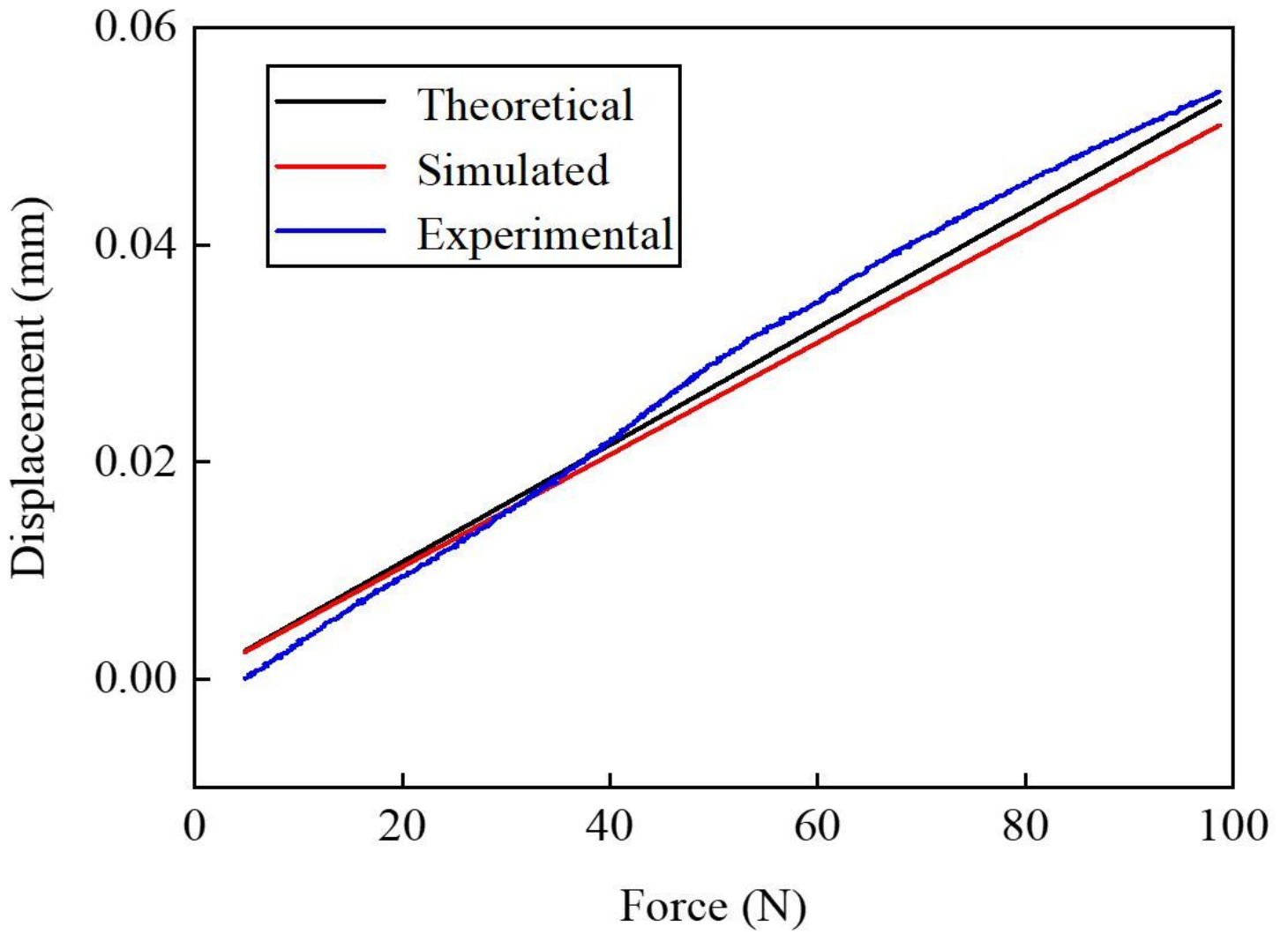


Figure 12

Force-displacement curve

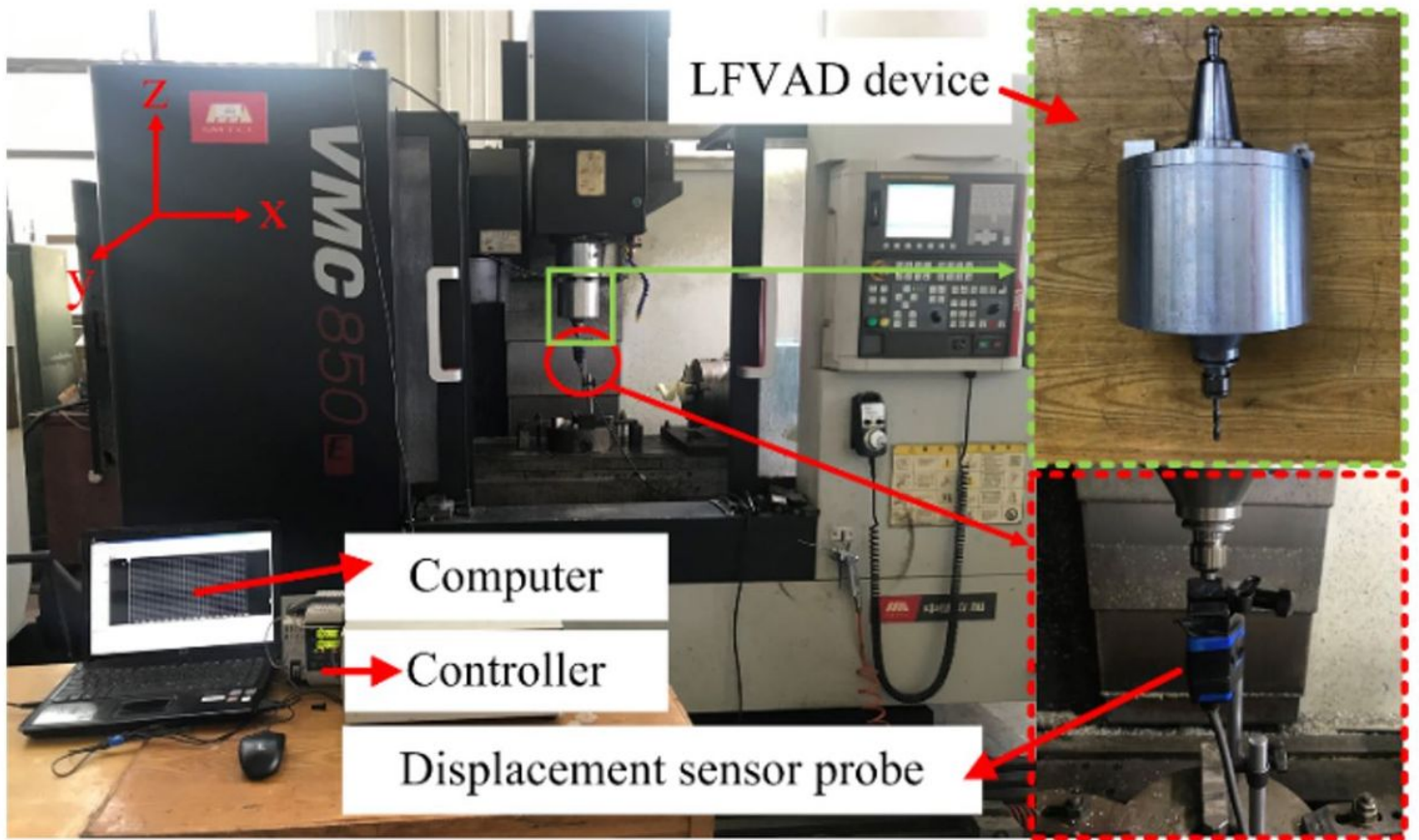


Figure 13

Vibration performance test site of the device

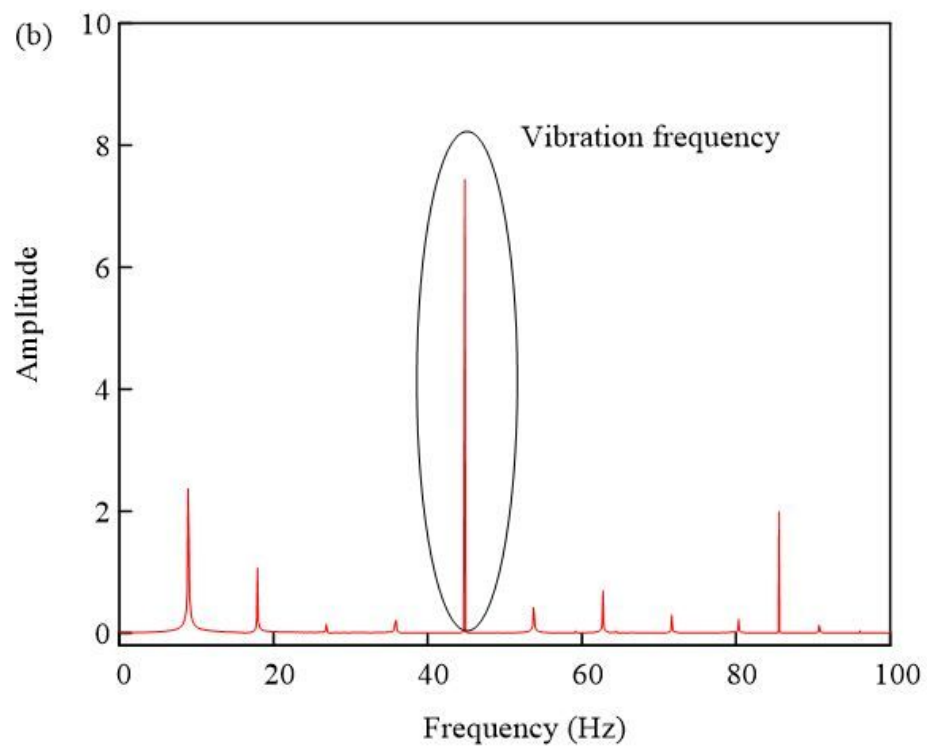
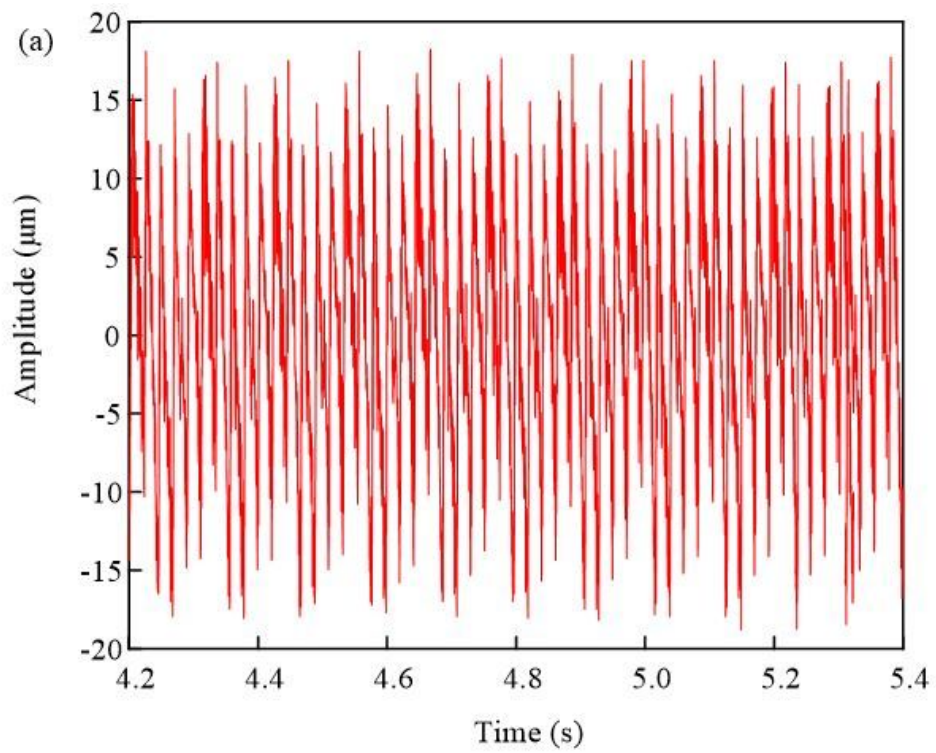


Figure 14

Low-frequency vibration test results: (a) time domain, (b) frequency domain

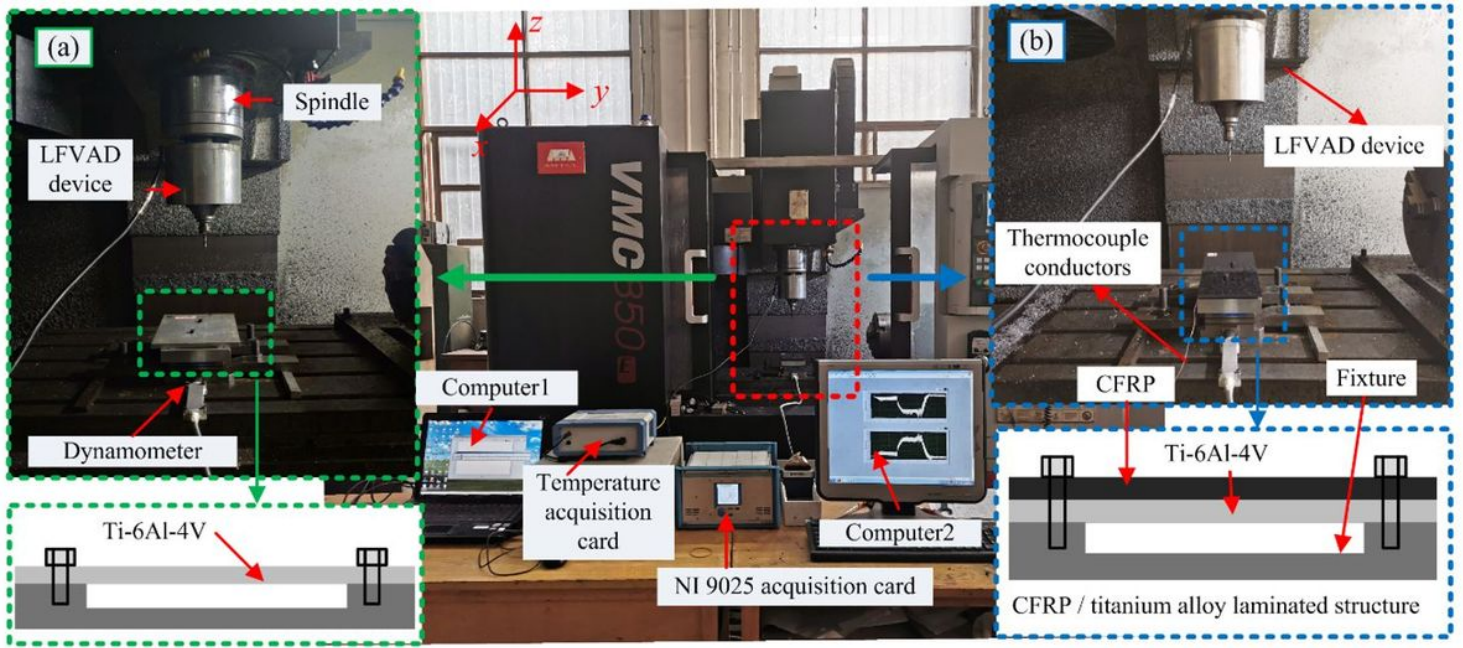


Figure 15

Drilling performance test

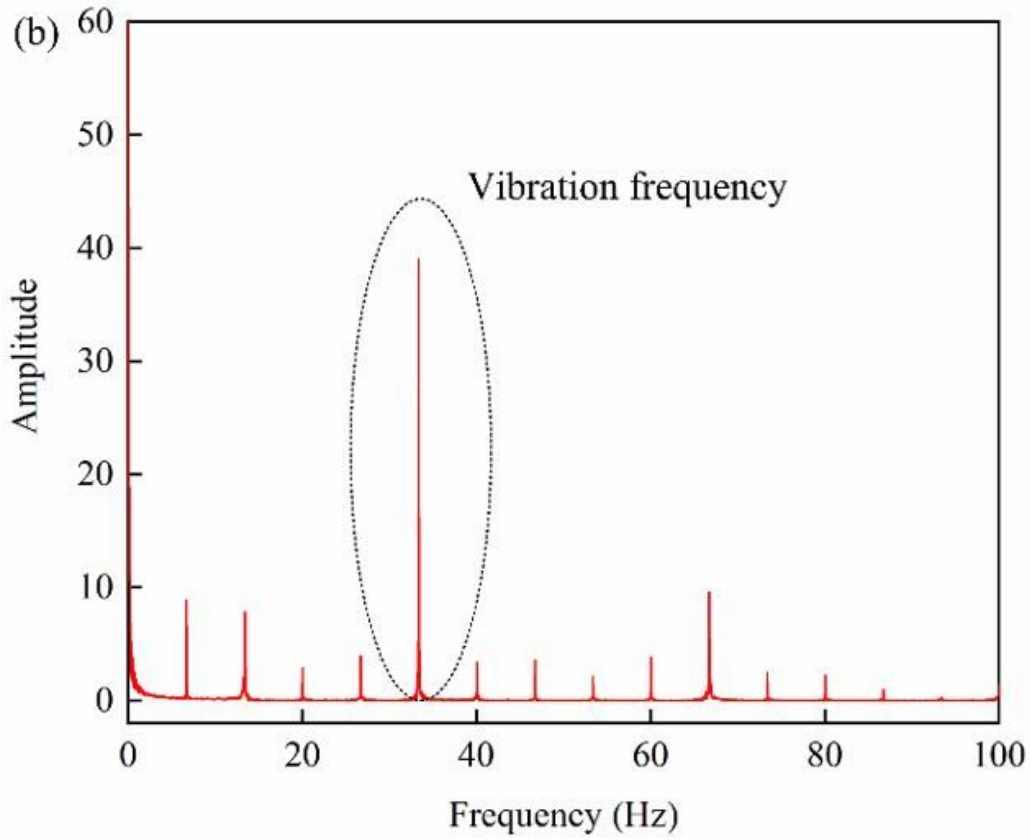
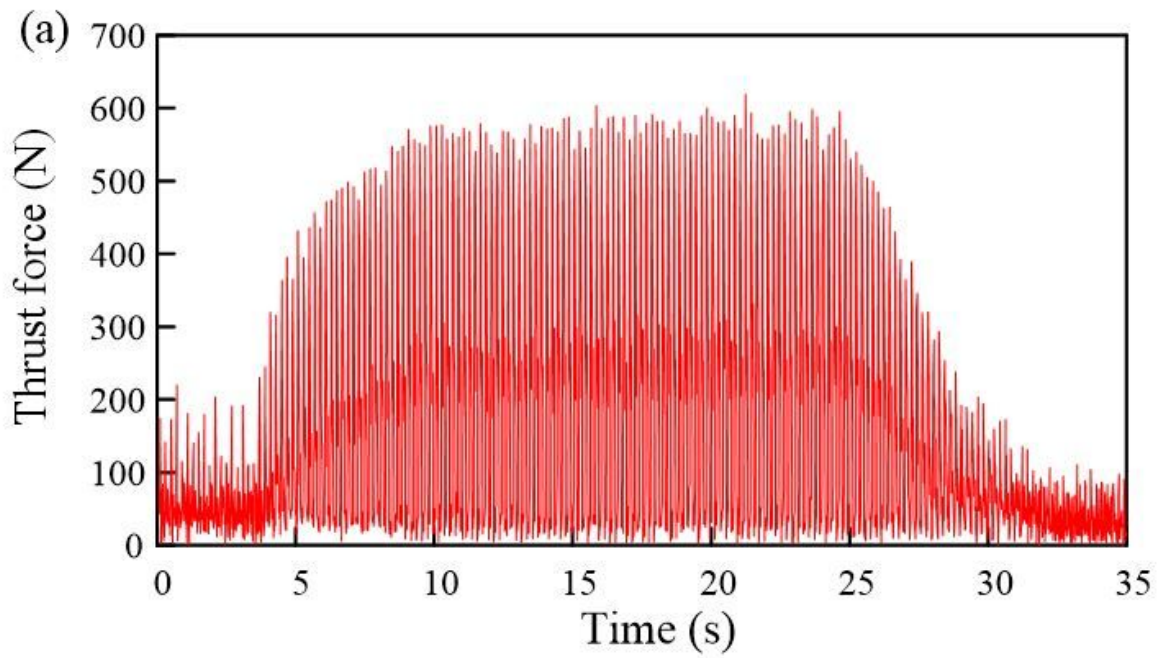


Figure 16

Drilling performance test

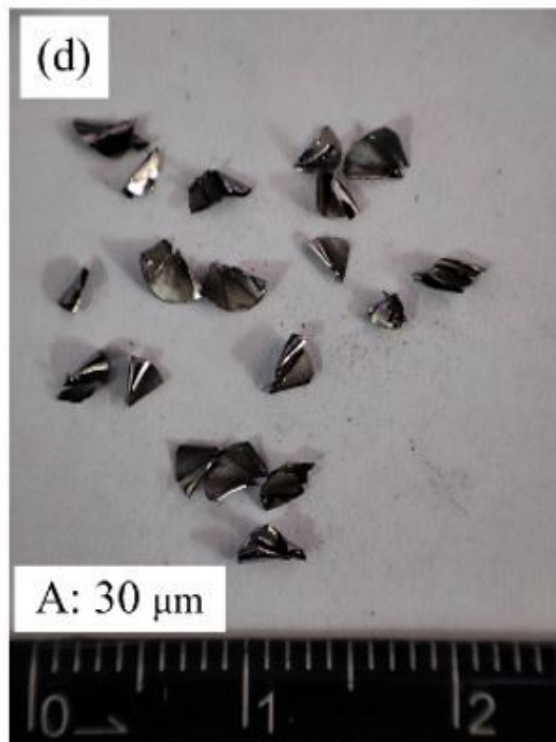
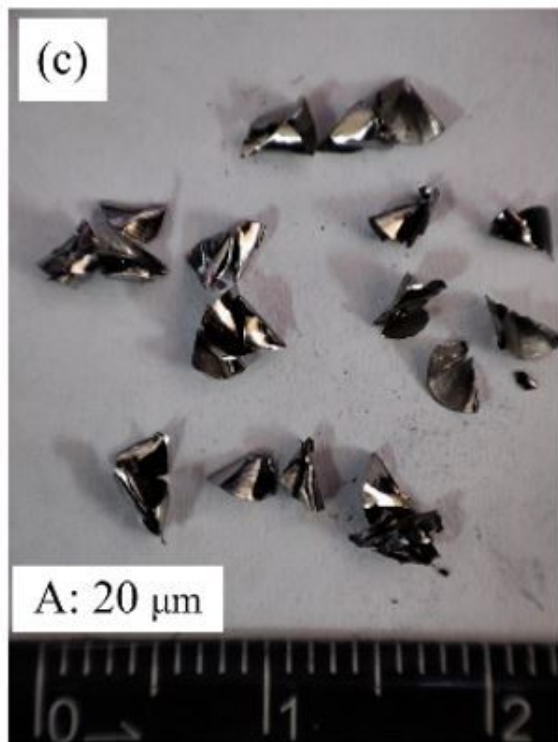
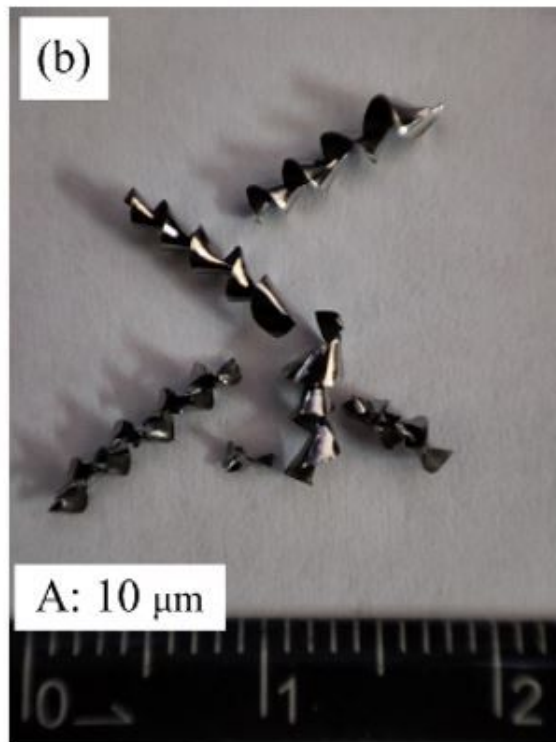
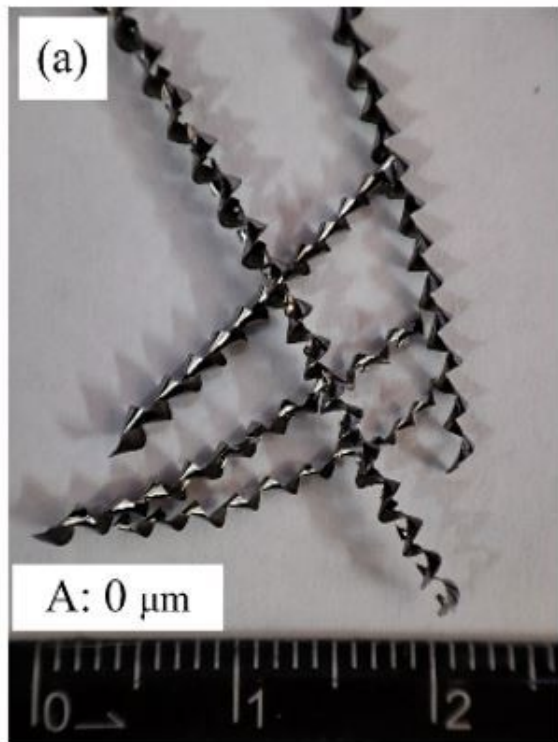


Figure 17

Chip morphology

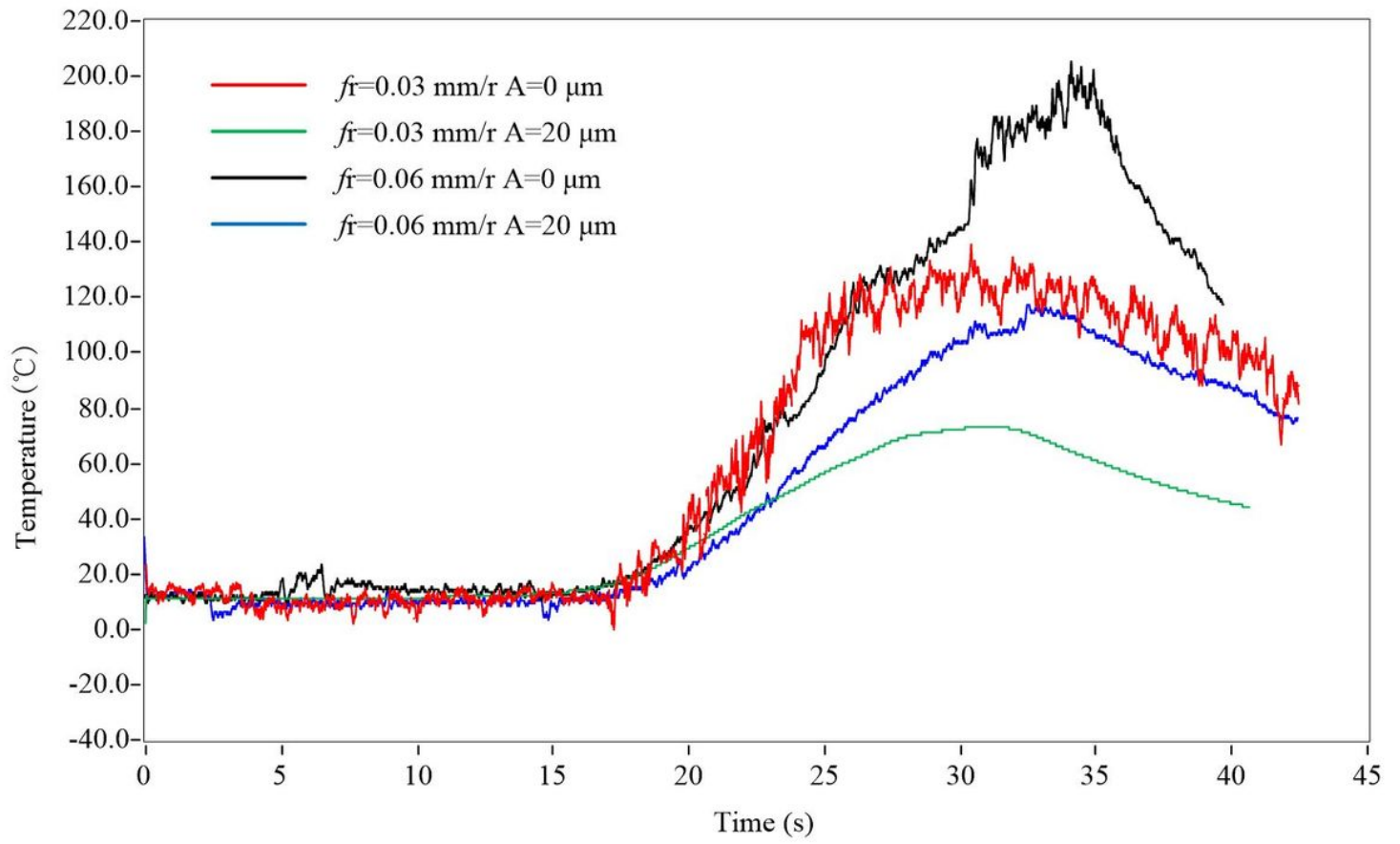


Figure 18

Temperature of drilling process

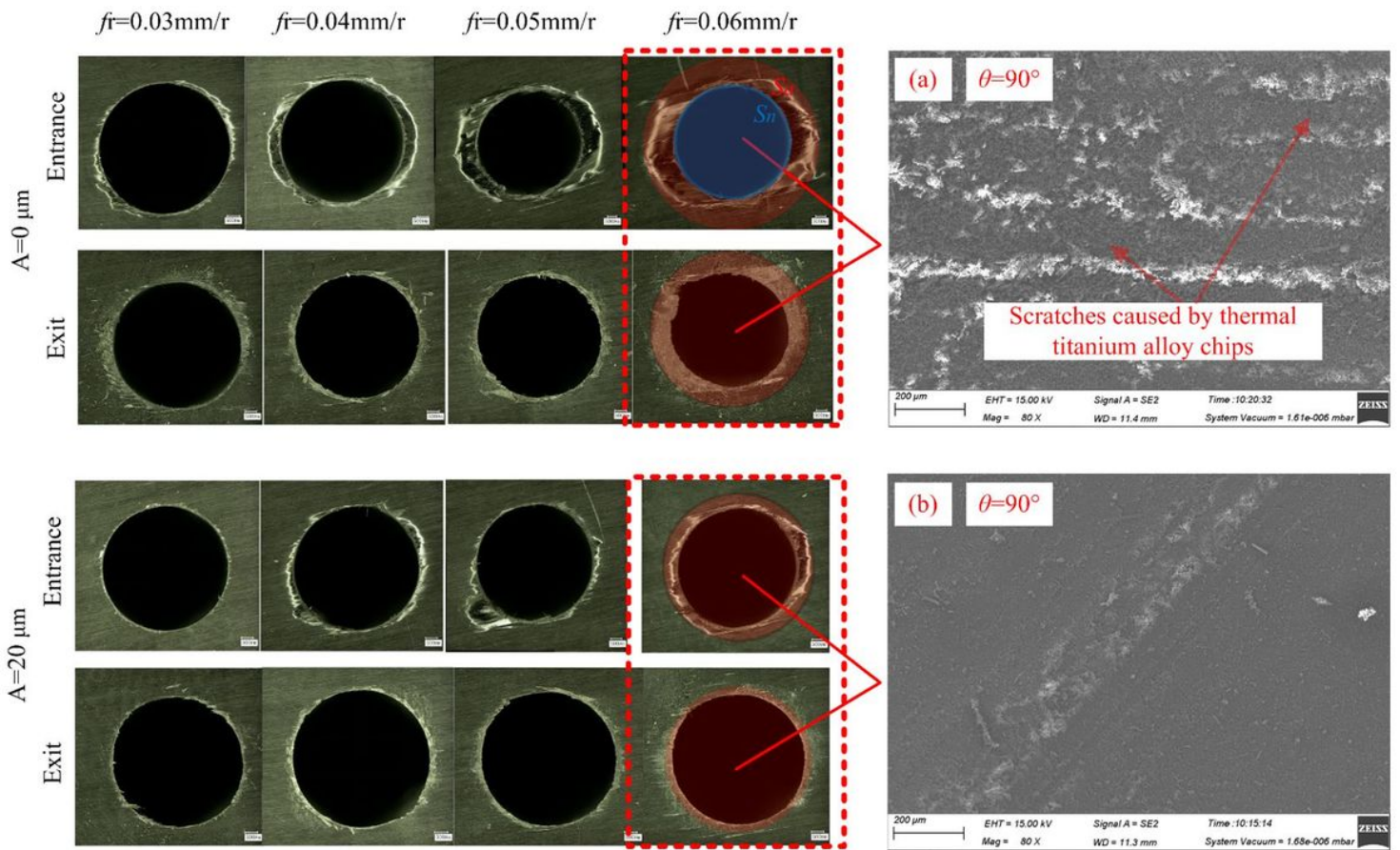


Figure 19

The entrance and exit morphology of CFRP

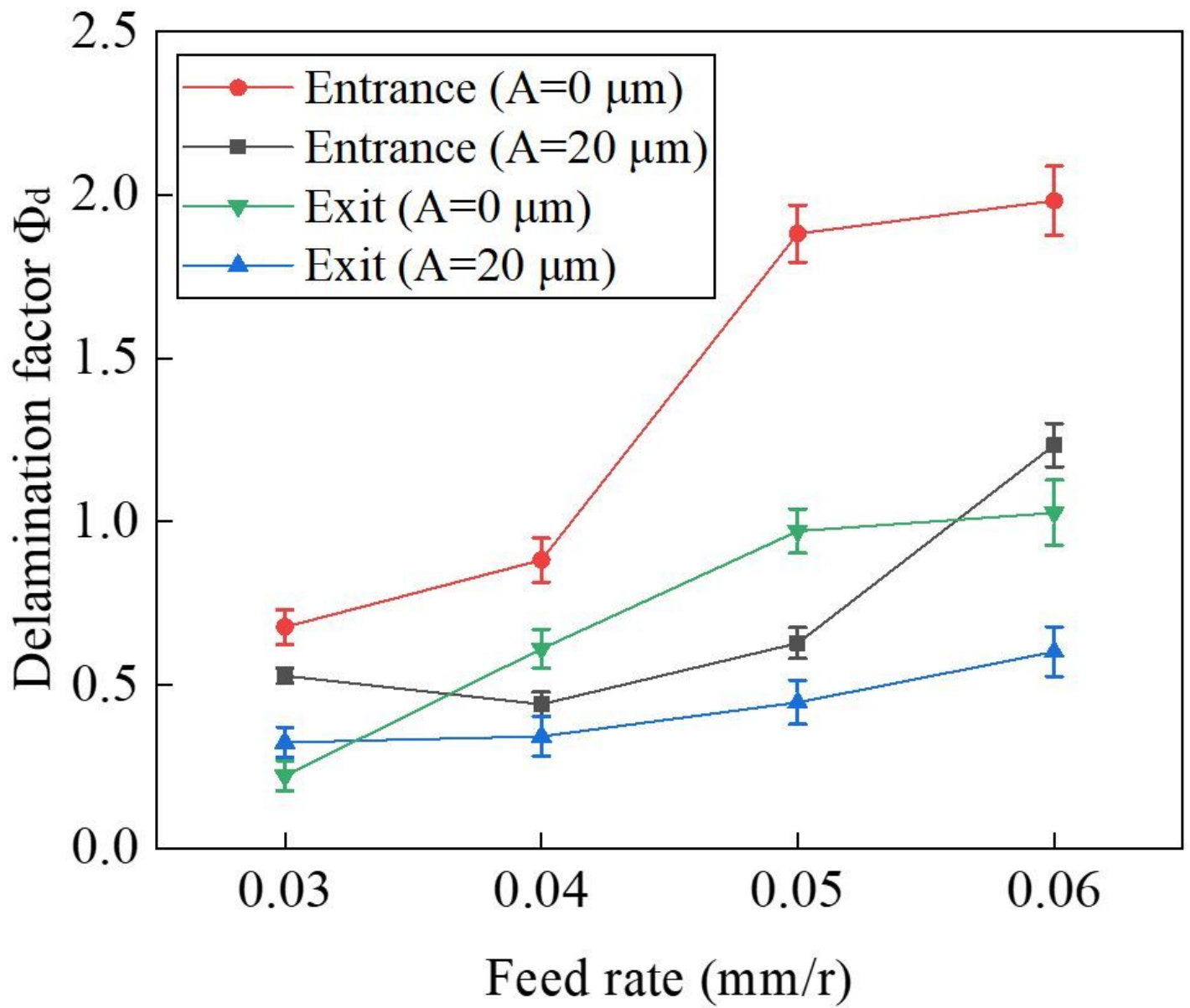


Figure 20

Delamination factor